Ore Geology Reviews 157 (2023) 105452

Contents lists available at ScienceDirect

Ore Geology Reviews

journal homepage: www.elsevier.com/locate/oregeorev

Metal source and ore precipitation mechanism of the Ashawayi orogenic gold deposit, southwestern Tianshan Orogen, western China: Constraints from textures and trace elements in pyrite

Zhenju Zhou [a,b,*], Zhengle Chen [a,b,c,*], Stefan Weyer [d], Ingo Horn [d], Hailong Huo [a,b], Wengao Zhang [a,b], Nuo Li [d,e], Qing Zhang [a,b], Fengbin Han [a,b], Hongye Feng [f]

[a] Institute of Geomechanics, Chinese Academy of Geological Sciences, Beijing 100081, China
[b] Key Laboratory of Paleomagnetism and Tectonic Reconstruction of Ministry of Natural Resources, Beijing 100081, China
[c] State Key Laboratory of Nuclear Resources and Environment, East China University of Technology, Nanchang 330013, China
[d] Institut für Mineralogie, Leibniz Universität Hannover, Callinstr. 3, 30167 Hannover, Germany
[e] Xinjiang Research Center for Mineral Resources, Xinjiang Institute of Ecology and Geography, Chinese Academy of Sciences, Urumqi 830011, China
[f] Key Laboratory of Computational Geodynamics, College of Earth and Planetary Sciences, University of Chinese Academy of Sciences, Beijing 100049, China

ARTICLE INFO

Keywords:
Orogenic gold deposit
Pyrite
Trace elements
Southwestern Tianshan
Ashawayi (W China)

ABSTRACT

The metal source and ore precipitation mechanism of orogenic gold mineralization are not yet well understood, partly because ore metals may be derived from different sources. Pyrite is a dominant Au-hosting mineral in the Ashawayi orogenic gold deposit in the southwestern Tianshan orogen, western China. Petrographic features of pyrite in host rocks and orebodies define four generations: diagenetic preore (Py1), hydrothermal early-ore (Py2), main-ore (Py3), and late-ore (Py4) pyrites.

Trace element abundances were analyzed in situ by femtosecond laser ablation inductively coupled plasma mass spectrometry (fs-LA-ICP-MS) to unravel the pyrite formation history. Preore Py1 contains the lowest Cu, Mo, Se, Au and As contents, consistent with a diagenetic origin. Py2 has higher Au and As contents than Py1 and may have formed by the reaction between hydrothermal fluid and preexisting Py1, as indicated by diagenetic pyrite-like As/Ni and Bi/Au ratios but lower hydrothermal pyrite-like Sb/Au ratios in Py2. Hydrothermal pyrite (Py3) contains more abundant As (1723–65182 ppm) and Au (0.32–107 ppm) but lower Co and Ni contents than Py2, suggesting a greater hydrothermal fluid contribution. Oscillatory zoning and abundant mineral inclusions (e.g., arsenopyrite and chalcopyrite) in porous Py3 indicate that fluid boiling was responsible for gold deposition during the main-ore stage. Py4 is a relict of hydrothermal pyrite (Py3) but not diagenetic pyrite, as supported by Py4 and Py3 clustering into a class based on hierarchical cluster analysis. The application of a machine learning method (i.e., artificial neural network) to the *syn*-ore pyrite indicates that the Ashawayi gold deposit has affinity to those from orogenic-type gold deposits worldwide. Our study, therefore, highlights that ore metals in orogenic gold deposits may originate from different sources, such as Au and As, which are largely sourced from metamorphic fluids, while Co and Ni are mainly released from preore sedimentary pyrite, fluid boiling and fluid-rock interaction triggered precipitation of Au and other metals.

1 Introduction

Orogenic gold deposits represent a major gold resource globally (Weatherley and Henley, 2013), and gold bodies are characterized by quartz-sulfide veins and an intimate relationship between sulfides and gold (Groves et al., 1998; Goldfarb et al., 2005; Chen, 2006, 2013; Augustin and Gaboury, 2019). It is widely accepted that unraveling metal sources and ore precipitation mechanisms in studies of orogenic gold deposits is significant for understanding gold mineralization processes and helping with developing exploration strategies (Voute et al. 2019; Chinnasamy et al., 2021; Yang et al., 2021). The mechanisms by which ore metals are extracted from source rocks are unclear. Most

* Corresponding authors.
E-mail addresses: zhenjuzhou@126.com (Z. Zhou), chenzhengle@263.net (Z. Chen).

https://doi.org/10.1016/j.oregeorev.2023.105452
Received 9 November 2022; Received in revised form 18 April 2023; Accepted 18 April 2023
Available online 22 April 2023

previously studied ore material sources can be constrained by the sulfur, lead, strontium and neodymium isotope compositions of sulfide minerals. However, pyrite, as a predominant sulfide mineral, can incorporate a wide range of trace elements (e.g., Au, As, Cu, Zn, Ag and Sb), which may originate from different sources. For example, Pitcairn et al. (2006) and Large et al. (2009, 2011) considered that preore stage pyrite (sedimentary and diagenetic pyrite) could be the source of Au (and As and S) for orogenic Au mineralization. Alternatively, Li et al. (2020b) suggested that Au and As come from hydrothermal fluids, while preore pyrite may supply other constituents (e.g., S, Bi, Mn, Co and Ni). Thus, it is important to determine the concentrations of Au and other metals in pyrite from the preore to *syn*-ore stages. Moreover, gold precipitation mechanisms have long been controversial, including fluid mixing (Brown, 1998; Graupner et al., 2001), fluid boiling (Hagemann and Luders, 2003; Li et al., 2018), fluid immiscibility and mixing triggered by pressure fluctuations (Matthai et al., 1995; Chen et al., 2012a, 2019), and fluid-rock interactions (Evans, et al., 2006; Yang et al., 2021).

Located on the northern margin of the Tarim Craton, the southwestern Tianshan orogen is an important component of the southwestern Central Asia Orogenic Belt (CAOB; Fig. 1a; Sengör et al., 1993). Many large and giant gold deposits have been identified in the southwestern Tianshan orogen in Uzbekistan, Tajikistan, Kazakhstan, Kyrgyzstan and NW China since the early 1980 s (Fig. 1b), such as the Muruntau (6137 t Au; Frimmel, 2008), Zarmitan (314 t Au; Abzalov, 2007), Daugyztau (186 t Au; Bierlein and Wilde, 2010), Jilau (110 t Au; Cole et al., 2000), and Swayaerdun (130 t Au; Liu et al., 2007) deposits. The Ashawayi gold deposit in the Chinese southwestern Tianshan shows features similar to those of the large Swayaerdun orogenic gold deposit. In this paper, we present new data on the deposit geology and fs–LA–ICP-MS pyrite trace element geochemistry from Ashawayi. Our aims are to unravel the (1) formation of the various generations of pyrite and any genetic link, (2) the source of gold and associated trace elements, and (3) the mechanism of ore metal precipitation and classification of the ore deposit type.

2 Regional geology

The Tianshan orogenic belt is bounded by the Junggar Basin to the north and the Tarim Basin to the south (Fig. 1a; Sengör et al., 1993; Kröner et al., 2014; Deng et al., 2017). From north to south, three tectonic units (Northern Tianshan, Central Tianshan, and Southern Tianshan) are recognized, which are bounded by the North Tianshan, Nikolave Line–North Nalati, Atbashi–Inlychek–South Nalati, and North Tarim (Kalatieke) faults, respectively (Fig. 1b; Gao et al., 2009; Zhang

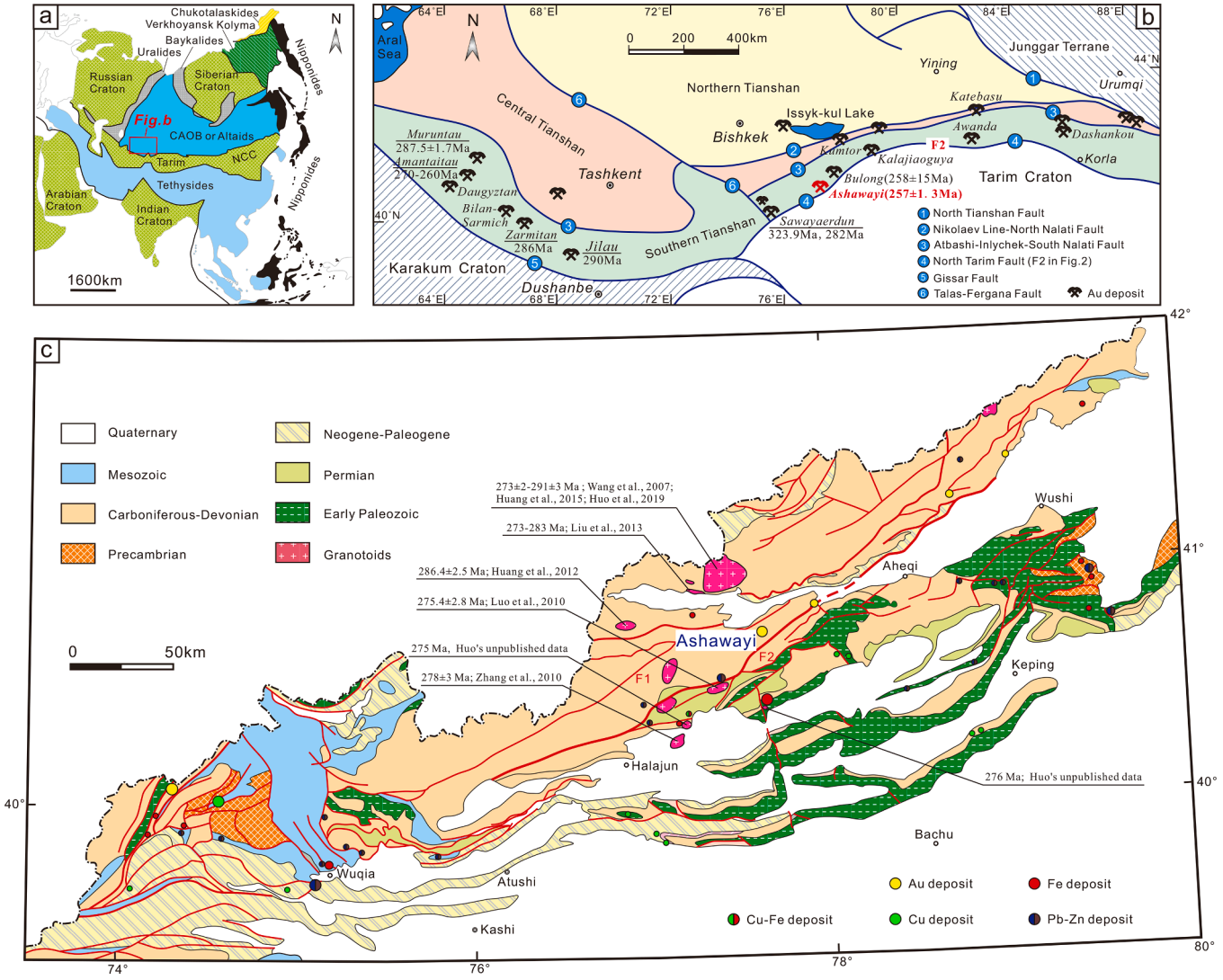

Fig. 1. a. Schematic map showing the location of the southwestern Tianshan orogen (modified after Sengör et al., 1993). Abbreviation: NCC = North China Craton; b. sketch map of the southwestern Tianshan orogen and adjacent regions (modified after Zhang et al., 2017); c. geologic map of the Chinese southwestern Tianshan orogen (modified after Dong et al., 2017).

et al., 2017; Chen et al., 2018). The southwestern Tianshan orogen extends across Uzbekistan, Tajikistan, eastern Kazakhstan, Kyrgyzstan and Xinjiang (NW China) and was formed by continent–continent collision between the Tarim and Kazakhstan–Yili blocks (Sengör et al., 1993; Ding et al., 2014; Zhou et al., 2018, 2019). Our study focused mainly on the Chinese section of the southwestern Tianshan (Fig. 1c).

The southwestern Tianshan orogen is bounded by the Yili–Central Tianshan arc to the north and the Tarim and Karakum Cratons to the south (Fig. 1b; Abuduxun et al., 2021). Since the late Paleozoic, the southwestern Tianshan has been affected by multiple orogenic events responsible for closure of the South Tianshan Ocean. The estimated time of final closure of the South Tianshan Ocean varies from the Middle Devonian–late Carboniferous (Charvet et al., 2007; Han et al., 2011; Alexeiev et al., 2015) to the late Permian-Triassic (Xiao et al., 2013; Sang et al., 2020; Abuduxun et al., 2021; Tan et al., 2022). The Chinese southwestern Tianshan orogen consists mainly of Precambrian metamorphic rocks, a lower Paleozoic sedimentary sequence, and a late Paleozoic to Mesozoic accretionary wedge and ophiolite belt. These geological units record the history of Precambrian paleocontinental nucleus formation and subsequent oceanic crust subduction and collisional orogenic events (Chen et al., 2018, 2021; Abuduxun et al., 2021). Precambrian units are locally exposed in the southwestern Tianshan (Fig. 1c), mainly comprising gneiss, schist, granulite and quartzite with minor tillite and clastic rocks. The lower Paleozoic strata comprise marine carbonate (limestone and dolomite) and clastic (sandstone–slate) rocks and are widely developed in the region. Devonian–Carboniferous rocks comprise submarine volcanic–sedimentary sequences, including phyllite, sandstone–mudstone, limestone/dolomite/marble, and intermediate–mafic volcanic/volcaniclastic rocks. The Permian strata are mainly composed of basalt, andesite, tuff, terrestrial glutenite, and siltstone–mudstone. Mesozoic strata mainly consist of lacustrine/fluvial clastic rocks with local coal seams and continental volcanic rocks, probably developed in intermontane and foreland basins (Yang et al., 2007; Chen et al., 2018). The Paleogene–Neogene sequences are characterized by red gypsum-bearing fluvial and lacustrine sediments.

Precambrian and lower Paleozoic lithostratigraphic units in the region are commonly intruded by Permian granitoids, such as the Chuanwulu (286.4 ± 2.5 Ma; Huang et al., 2012), Halajun (278 ± 3 Ma; Zhang et al., 2010) and Baleigon (273 ± 2 Ma to 291 ± 3 Ma; Wang et al., 2007; Huang et al., 2015; Huo et al., 2019) plutons (Fig. 1c). Furthermore, 298–260 Ma granitoids have been reported in the Uzbekistan and Kyrgyzstan sections of the southwestern Tianshan (Solomovich and Trifonov, 2002; Mao et al., 2004; Konopelko et al., 2007; Seltmann et al., 2011). These granitoids represent postcollisional magmatism in the southwestern Tianshan, which constrains the timing of the Tarim–Kazakhstan continent–continent collision, and the southwestern Tianshan Ocean closure likely occurred before the Permian (Gao et al., 2011; Seltmann et al., 2011).

During the late Paleozoic, large-scale nappe tectonics and shearing occurred in the southwestern Tianshan, forming ductile–brittle structures (Gao et al., 1997). Huo (2019) presented a detailed structural analysis of these fault systems and concluded that the nappe tectonics were coeval with the pre-Permian syncollisional crustal thickening. The nappes were then intruded by granites and diabase, and shearing developed with Permian postcollisional crustal thinning. Deformation fabrics in the tectonic zones consist of "M"- and "Z"-type folds, with local thick top fold and cleavage development, indicating a change from ductile to brittle deformation. Undeformed diabases (zircon U-Pb age: 295–240 Ma) intruded folds at Biedieli and Kepingduanlong in NW Xinjiang, suggesting that brittle–plastic deformation occurred before the late Paleozoic (Huo, 2019). These ductile–brittle shear zones and faults are the most favorable sites for localizing orebodies and granitoids.

More than ten gold deposits are present in the Chinese southwestern Tianshan orogen. Zhang et al. (2017) constrained the Sawayaerdun gold mineralization to be ca. 324–282 Ma, based on pyrite re-Os isochron ages of 323.9 ± 4.8 Ma (early ore stage) and 282 ± 12 Ma (main ore stage). Zhao et al. (2002) reported a quartz Rb-Sr isochron age of 258 ± 15 Ma for the Bulong deposit. Recently, we obtained a quartz Rb-Sr isochron age of 257 ± 1.3 Ma for the Ashawayi deposit (Zhou's unpublished data). Many world-class gold deposits of similar ages have been discovered in the southwestern Tianshan orogen outside China, notably Muruntau (287.5 ± 1.7 Ma; Mörelli et al., 2007) and Zarmitan (286 Ma; Goldfarb et al., 2014). This distribution suggests that the southwestern Tianshan gold belt was intensely involved in a late Paleozoic tectonic–metallogenic event (Xue et al., 2014, 2020; Chen et al., 2012a, b; Zhou et al., 2019).

Other types of mineral deposits also developed in the sedimentary sequences of the Chinese southwestern Tianshan orogen, e.g., Cu and Pb-Zn deposits (Fig. 1c). Two principal styles of Pb-Zn deposits occur in the district: Mississippi Valley-type (MVT) and sandstone-type deposits. The Cu deposits (e.g., Sareke, Jiashi and Dishui) in the district are mainly sandstone-type systems developed in Mesozoic–Cenozoic sandstone–conglomerate strata (Li et al., 2011; Wang et al., 2018a, b; Zhao et al., 2018).

3. Deposit geology

3.1. Lithologic units and structural geology

The Ashawayi gold deposit is located in the western part of the southwestern Tianshan gold belt (Fig. 1c). In 2003, the No. 8 team of the Xinjiang Bureau of Geo-exploration and Mineral Development (BGMR) carried out regional geological field mapping and lithochemical sampling of the Ashawayi deposit, leading to the discovery of two mineralized bodies. Recent geological/geophysical surveys and drilling by the current owner (Sinomine Resource Exploration Co. ltd.) resulted in the discovery of 42 gold ore lenses, yielding a total reserve of>5 t Au and an estimated resource of>10 t Au @ 1.57 g/t. The Ashawayi gold deposit hosts the Yuqikai and Ashawayi sections in its western and eastern parts, respectively (Fig. 2). There are approximately 50 gold ore lenses in the Yuqikai and Ashawayi sections (Fig. 3). Gold ores in the Ashawayi deposit can be divided into primary ores and oxidized ores (Zhang et al., 2020). The oxidized ores are yellow in color and have vuggy or honeycomb structures. They crop out mainly in the eastern part of the deposit and are distributed in the upper ~ 150 m below the current ground surface. The primary ores are mainly composed of quartz–sulfide veins and occur below a depth of ~ 150 m. Oxidized ores account for < 10 % of the ore resources (Sinomine Resource Exploration Co. ltd., unpublished report). At present, the Ashawayi gold deposit has not been exploited.

There are three major sedimentary units at Ashawayi: the lower Carboniferous Aiktike Formation sandstone–silicolite interbeds, the upper Carboniferous Kalachirga Formation (main ore host) low-grade *meta*-sandstone–mudstone and phyllite interbeds, and Quaternary sediments (Figs. 3, 4).

The Ashawayi deposit is located between the Kalatiebieke and Kalatieke faults (Fig. 2). NE- and N—S—trending subsidiary faults are recognized in the sections. The NE-trending faults are consistent with the regional tectonic pattern and crosscut the strata. These faults have ductile to brittle features and controlled the gold veining (south-dipping at a dip angle of 40°). Gold-barren quartz veins occur parallel to the wallrock schistosity (Fig. 5a), while fractured auriferous quartz veins occur not only along the phyllite schistosity (Fig. 5a) but also as lenses in the phyllite (Fig. 5b). In addition, en echelon quartz veins (Fig. 5c), fault gouge and breccia (Fig. 5d) are present in the ore-bearing fracture zones in Adit No. 5 (abbrev. PD5) (Fig. 3).

3.2 Gold orebodies

The Ashawayi gold ores are mainly auriferous quartz vein-type and minor altered wallrock-type ores. The auriferous quartz veins are hosted

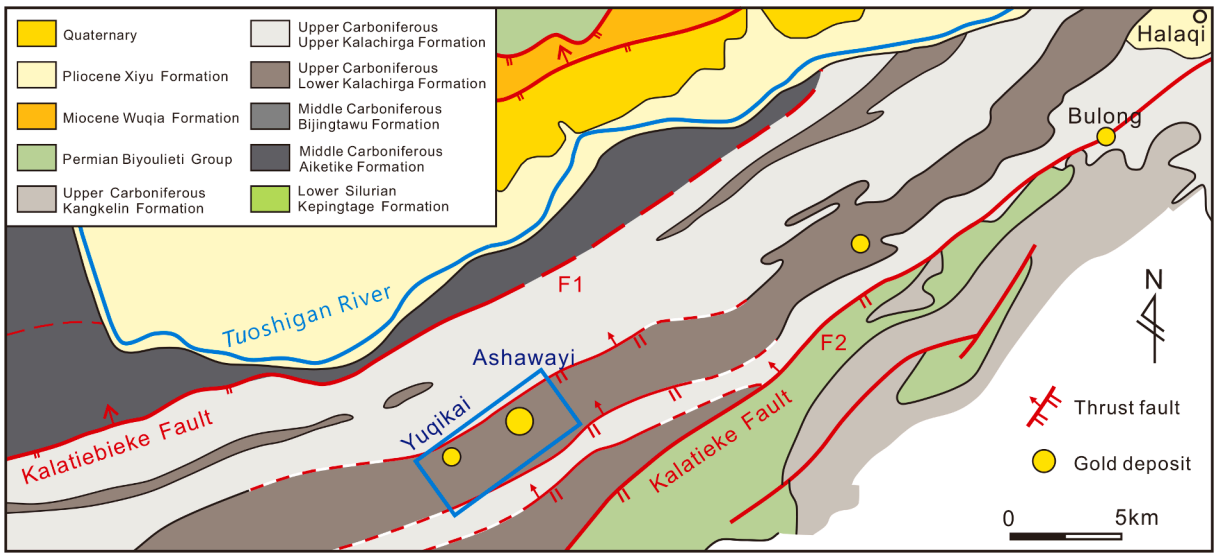

Fig. 2. Regional geological map of the Ashawayi gold deposit (modified after Chen et al., 2007).

in altered fracture zones (Fig. 4), in which the veins are parallel to or crosscut the wallrock schistosity (Fig. 5a, b), forming local tectonic breccia (Fig. 5d). These veins strike NE (NW-dipping with dip angles of 60–86°) and are 100–1000 m long and 0.27–8.91 m thick. The ore lenses occur as veins or lenses in fractured alteration zones (Fig. 5a-d) and locally in interlayer fracture zones between the carbonaceous phyllite and sandstone. High-grade orebodies are preferentially distributed in jogs, bends, bifurcations, and splays, which indicates that vein interconnection played an important role in fluid flow and gold precipitation (Garofalo et al., 2002).

Microstructural faults also display ductile to brittle deformation in hand specimens and petrographic thin sections. Microscopic images of quartz show directional stretching and undulose extinction formed by ductile deformation (Fig. 5g). Fracturing is observed in smoky gray quartz veins (Fig. 5e). In some cases, the smoky gray quartz grains have undergone brittle deformation and are fragmented along their edges, with weak undulose extinction (Fig. 5h).

3.3 Ore mineralogy

The main ore mineral is pyrite, and other minor metallic minerals include arsenopyrite, stibnite, chalcopyrite, galena, sphalerite, magnetite, and limonite. Nonmetallic minerals include quartz, feldspars, sericite, muscovite, chlorite, ankerite, calcite, apatite, and monazite. Gold occurs mainly as invisible gold in pyrite. Pyrite is present as thin veinlets and disseminations in the alteration zones. According to the morphology, texture, and mineral association, four generations of pyrite can be identified in the Ashawayi deposit (Table 1): (1) preore framboidal or fine-grained euhedral pyrite (Py1) is present in the sedimentary rocks of the Kalachirga Formation (Fig. 6); (2) early-ore subhedral–anhedral fine-/medium-grained pyrite (Py2) cores overgrown by later main-ore pyrite rims (Fig. 7a, b); (3) main-ore coarse pyrite (Py3) grains or aggregates associated with gray quartz, arsenopyrite, chalcopyrite, and stibnite (Fig. 8); and (4) late-ore pyrite relicts (Py4) in yellow oxidized ores (Fig. 5f, 9f, g).

Arsenopyrite grains (size: 30–500 μm) are generally acicular, rhombic, or prismatic (Fig. 8a, b). They are randomly disseminated throughout the altered rock matrix and in quartz veins. Arsenopyrite occurs as inclusions in Py3 (Fig. 7c), overgrows Py3, or is overgrown by stibnite.

Chalcopyrite (size: 10–400 μm) is mainly anhedral to subhedral (Fig. 8c) and occurs as disseminations or inclusions in Py3 (Fig. 8d). It also occurs locally around main-ore pyrite and quartz grains or as fracture infills in these minerals.

Stibnite is generally coarse-grained (size: 0.2–4 mm, up to 3 cm) and anhedral–subhedral (Fig. 8e, f). It occurs dominantly in quartz veins, and some stibnite grains are broken and replace pyrite and arsenopyrite (Fig. 8e, f).

3.4 Hydrothermal alteration

In the Ashawayi deposit, wallrock alteration is widespread and includes silicic, sericite, carbonate, and sulfide alterations. Gold mineralization is closely associated with pyritization and silicification, the latter being multistage and the most pervasive (Fig. 5a-d). Early-stage silicification occurred as Au-barren quartz veins along the phyllite foliation, and the quartz is milky to gray and exhibits ductile deformation features, such as directional stretching, undulose extinction, and ribbon-like texture (Fig. 5g). The second-stage silicification occurs mainly as auriferous quartz veins, and the quartz is smoky gray and precipitated with coarse-grained pyrite grains/aggregates, arsenopyrite, chalcopyrite, and stibnite (Fig. 8). These auriferous quartz veins are parallel to or cut the phyllite foliation (Fig. 5a, b). Late-stage weak silicification commonly occurs as quartz–calcite ± ankerite veinlets (with trace pyrite but no gold), which crosscut the earlier-formed quartz veins and altered wallrocks (Fig. 5j).

Sulfidation occurs as pyrite, along with arsenopyrite, stibnite and chalcopyrite. The sulfides occur as veinlets (Fig. 5e) or disseminations/aggregates in the host rocks and quartz veins. Sericite, altered from plagioclase and K-feldspar, is widely developed in both phyllite and sandstone and commonly associated with disseminated sulfides (Fig. 5g). Carbonate alteration mainly occurs as disseminated or veinlets of calcite and ankerite in the altered wallrocks (Fig. 5i, j).

4. Occurrence and texture of pyrite

Preore stage pyrite (Py1): Py1 is present in the phyllite and sandstone of the Kalachirga Formation, which is an important host rock. This type of pyrite can be subdivided into Py1a and Py1b: the former is extremely fine-grained (0.1–2 μm) and forms framboids that are 5 to 15 μm across (Fig. 6a, b), whereas the latter is much larger (Fig. 6c, d), with diameters between 30 and 160 μm. Py1a is identified only in drill holes (ZK16901 and ZK1602) in this study, and clusters are commonly associated with pore spaces and with quartz, sericite, and feldspar. Py1b is characterized by euhedral crystals and homogeneous compositions in scanning electron microscopy (SEM) and backscattered electron (BSE) images

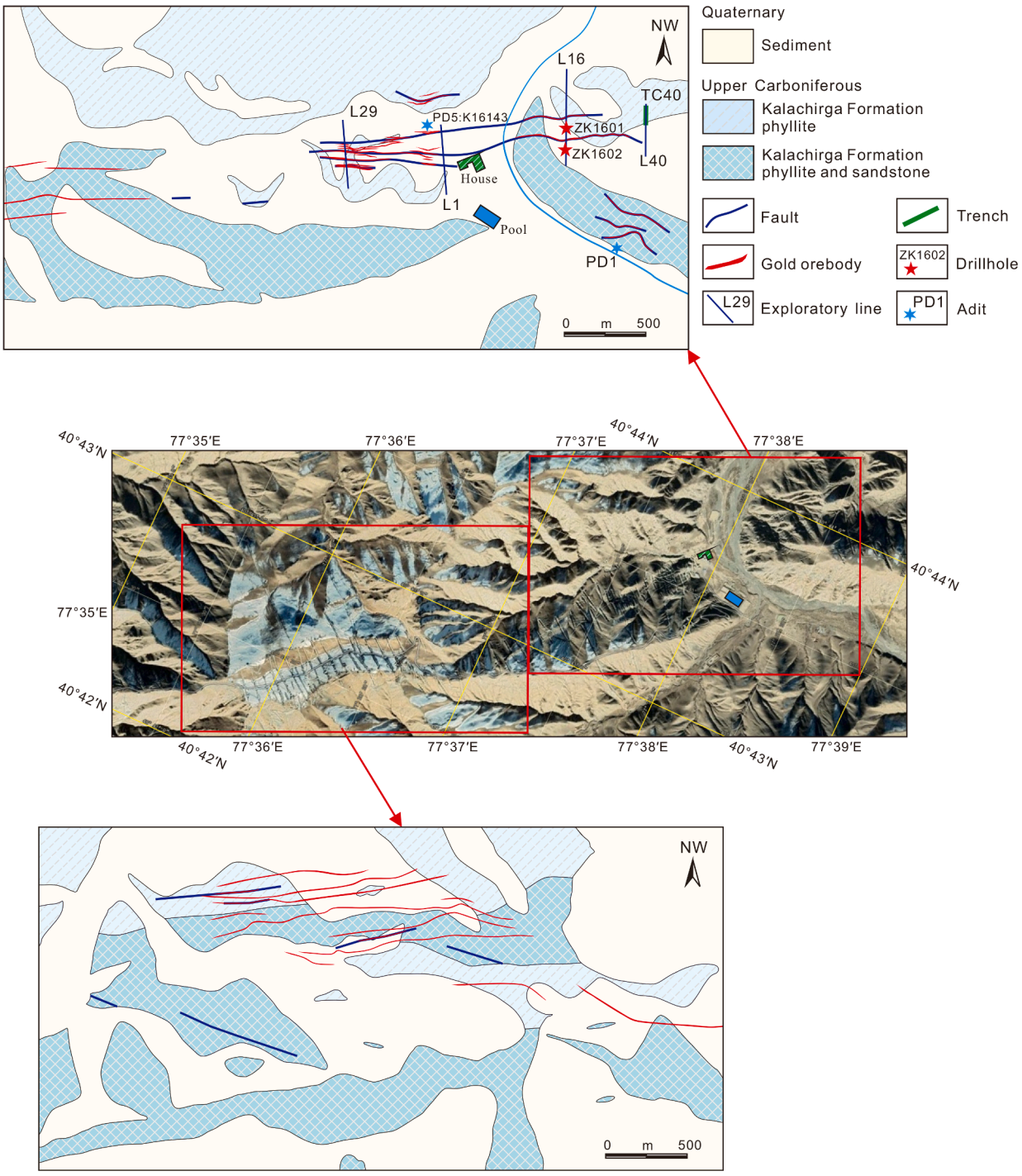

Fig. 3. Simplified geologic map of the Ashawayi gold deposit (modified after Chen et al., 2019), showing the surface projections of deep orebodies and faults.

(Fig. 6d). Some Py1b is overgrown by Py3 (Fig. 6c), which was modified by later hydrothermal fluid and thus was not selected for fs-LA–ICP-MS analysis.

Early-ore stage pyrite (Py2): Pyrite 2 has subhedral to euhedral cores (40–350 μm) (Fig. 7a) with overgrowth Py3a rims (Fig. 7b). Sharp boundaries and corrosion textures occur between the Py2 core and Py3a rim (Fig. 7a, b), and the core appears darker in BSE images. Some Py2 grains retain Py1 cubic crystals (Fig. 7a, b).

Main ore stage pyrite (Py3): Pyrite 3 is coarser-grained than both Py1 and Py2, varying from 50 to 1000 μm and mostly > 100 μm. Py3 shows associated relationships with gray quartz, arsenopyrite, stibnite and chalcopyrite (Fig. 7c, d, 8). Many Py3 grains are fragmented and porous (Fig. 7a), with microfissures (Fig. 7f). Locally, quartz pressure shadows adjacent to Py3 are observed (Fig. 7e), which suggest that Py3 was formed during deformation. Py3 can be further subdivided into Py3a, Py3b, Py3c and Py3d.

Py3a occurs as anhedral to subhedral rims that commonly surround and overgrow Py2 (Fig. 7a, b). Py3b consists of subhedral grains with oscillatory compositional zonation and arsenopyrite inclusions (Fig. 7c). Py3c is present as anhedral to euhedral grains and clusters without zoning (Fig. 8a, b). These pyrite grains commonly occur parallel to the early cleavage in phyllite and sandstone (Fig. 9a, b, e) or are randomly disseminated in carbonaceous phyllite and quartz veins (Fig. 9a-c).

Py3d in the late main ore stage occurs as subhedral–euhedral grains

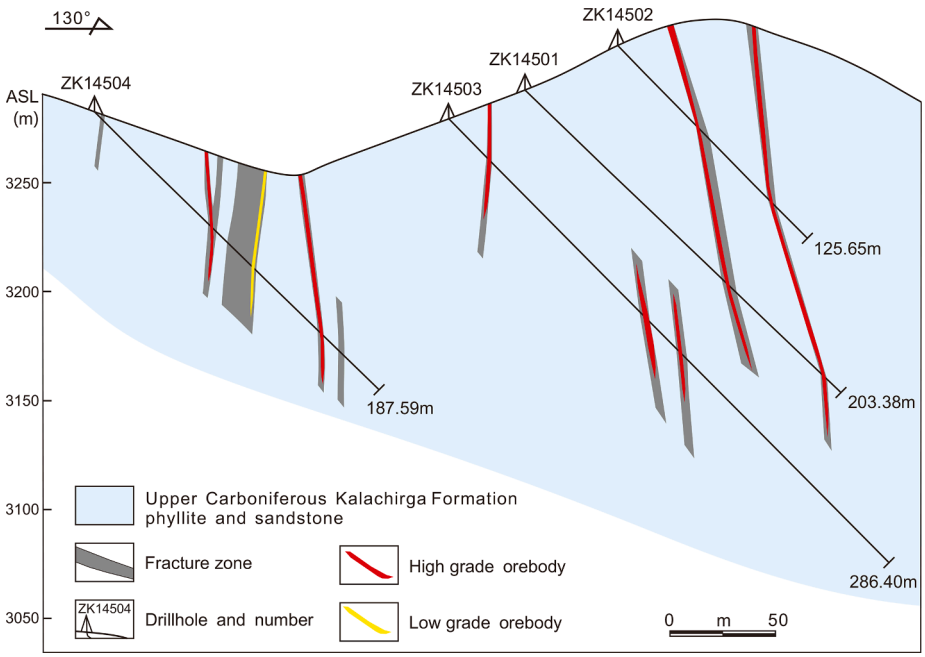

Fig. 4. Geologic section of the No. 145 prospecting line at the Ashawayi gold deposit.

(size: 60–250 μm) and is much less porous or fractured than Py3c (Fig. 9d). It forms veinlets with quartz cutting Py3c (parallel to late cleavages in the host rocks) and has no quartz pressure shadows (Fig. 9a, b), suggesting post-tectonic formation. SEM–BSE imaging reveals that Py3d is relatively homogeneous, without discernible zonation (Fig. 9d).

Late ore stage pyrite (Py4): Pyrite 4 (20–200 μm) in the late ore stage occurs as relicts of earlier pyrite (Fig. 9f, g) and is disseminated in the oxidized ores. Py4 is broken and homogeneous in BSE images. Limonite occurs in fissures of preexisting pyrite.

5. Samples and analytical methods

Samples for textural and chemical analyses were collected from field outcrops and from drill cores (ZK1602 and ZK1601). Mineralogical and textural studies were conducted on 11 polished thin sections, on which 261 spots were analyzed by in situ LA–ICP-MS for trace element geochemistry, and 104 of them were used in the study. The analyses that showed irregular transiet ablation signals where excluded, because these analyses are likely affected by mineral inclusions in pyrite. Trace element concentrations in pyrite were determined with fs–LA–ICP-MS at Leibnitz University Hannover (Germany) using He as the carrier gas in the ablation chamber. The laser ablation system was built based on a Spectra-Physics Solstice femtosecond laser operating in deep UV light at 194 nm, and the regenerative amplified system was pumped at 500 Hz, generating a pulse energy of 70 μJ in deep UV. Analytical techniques followed those described by Horn et al. (2006). A Thermo Element XR was used for analysis, operating in low-resolution mode without using the guard electrode. Nickel X-cones and a jet-sampler were also used for analysis. The total analysis time for each sample was 120 s, including approximately 45 s background acquisition (gas blank) and 75 s sample data acquisition (laser on). For this study, all analyses were performed with spot sizes of 30 to 60 μm. To monitor the quality of the analyses, reference materials ARM-1 (synthetic glass standard, Chinese Academy of Science) were analyzed. The calibrations used SRM NIST 610 as external and Fe as internal standards. For a detailed description, see Ciazela et al. (2018). Offline selection and integration of background and analyte signals and time-drift correction and quantitative calibration were performed by ICPMSDataCal (Liu et al., 2008). The mean detection limits were 0.01–0.06 ppm for Sc, V, Ag, Sb, W, Au, Tl, Pb, and Bi; 0.25–0.91 ppm for Mg, Al, Ti, Ni, Mn, Cu, Mo, and Zn; and 1.11–4.52 ppm for Na, Cr, Co, As and Se.

6. Results

Except for Py1a grains that are too small to analyze, the trace element contents of Py1b without evidence of metamorphic and hydrothermal influences, Py2, Py3, and Py4 were determined with fs-LA–ICP-MS, and the results are listed in Table S1 and Table 2. In general, the Ashawayi pyrite grains have Ti, Co, Ni, Cu, As, Pb and Bi concentrations that are above the detection limits, whereas the concentrations of other trace elements, including Mg, Al, V, Zn, Se, Mo, Ag, Sb, W, Au and Tl, with a few exceptions are below the detection limits (Table S1). The reported average and median values for trace elements are calculated by assigning all the analyses that are below the detection limit (bdl) to half of the corresponding detection limit values (Table 2). Trace elements with bdl concentrations are shown as half of the detection limit values for the LA–ICP-MS instrument on the diagrams (Figs. 10-13). The elemental correlations for pyrite were determined by principal component analysis (PCA) using PAST software. PCA allows the visualization of multidimensional (multielement) data on particularly useful planes by identifying orthogonal directions in the data that produce maximum variance (i.e., linear combinations; Winderbaum et al., 2012; Kerr et al., 2018; Román et al., 2019).

Py1 has low concentrations of Au (bdl-0.34 ppm), As (49.4–240 ppm), Cu (1.37–13.2 ppm), and Se (bdl-6.18 ppm) (Table 2; Fig. 10). PCA confirms that Au is strongly positively correlated with Cu–Pb–Sb–Bi and weakly associated with As (Fig. 11a). Compared to Py1, Py2 is rich in Au (0.02–4.22 ppm), As (35.5–31006 ppm), Cu (9.35–81.0 ppm), Se (3.98–12.5 ppm), and Bi (5.09–105 ppm) (Fig. 10). Furthermore, unlike Py1, Py2 contains only two elements (i.e., As and Cu) that show strongly positive correlations with Au (Fig. 11b).

Py3 has higher and more variable concentrations of most trace elements than the other types of pyrite (Fig. 10). Generally, for the same pyrite grain or cluster, the rim (Py3a) is brighter in BSE images and has higher Au, As, Cu and W (but lower Co, Ni, Bi, and Pb) contents than the core (Py2) (Table 2; Table S1), suggesting that the rims were formed from a different fluid from that of the cores. The Au and As concentrations in Py3a are 2.94–26.4 ppm (median of 12.2 ppm) and

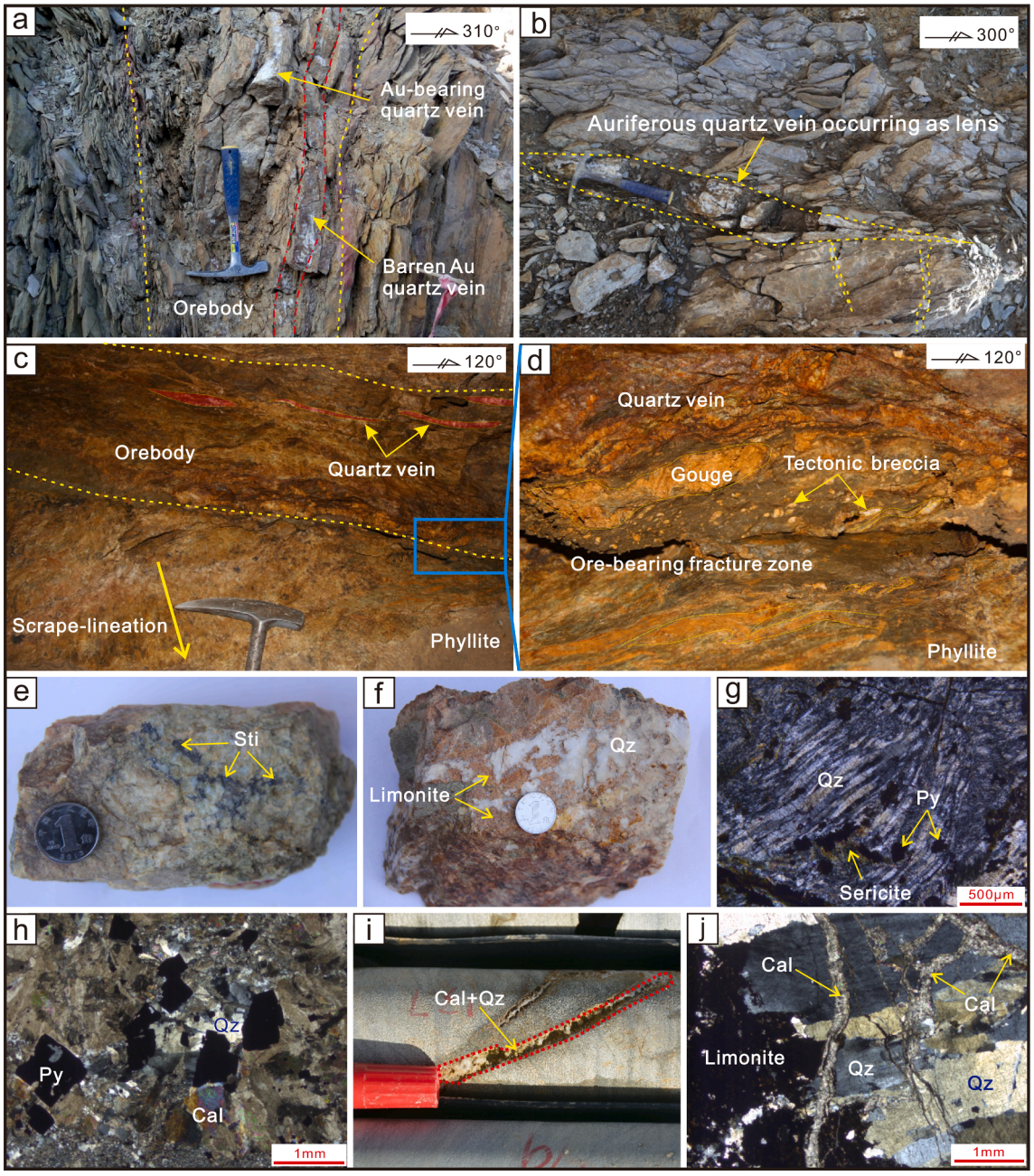

Fig. 5. Photographs of field and hand specimens, showing the Ashawayi gold mineralization and ore textures. a. Barren quartz vein parallel to the schistosity of host rocks; b. lensoidal auriferous quartz vein in phyllite; c. en echelon quartz veins in phyllite in PD5; d. quartz vein, gouge and tectonic breccia in an ore-bearing fracture zone in PD5; e. primary ore and stibnite (Sti) veinlets in quartz vein; f. yellow oxidized ore; g. transmitted light (TL; right) image of quartz, showing stretching and undulose extinction due to ductile deformation; h. cogenetic pyrite, quartz and calcite in the main ore stage; i. quartz–calcite veinlets; j. quartz–calcite veinlets crosscutting the earlier-formed quartz veins. (For interpretation of the references to color in this figure legend, the reader is referred to the web version of this article.)

20497–35337 ppm (median of 26068), respectively. As shown in Fig. 11c, Au in Py3a is positively correlated with Fe but negatively correlated with As and Cu.

The oscillatory zoned Py3b has significantly higher Au (median of 61.8 ppm), As (median of 38070 ppm), and Cu (median of 344 ppm) contents than the other types of pyrite (Table 2; Fig. 10). Gold in Py3b is strongly positively correlated with Cu but weakly associated with As (Fig. 11d). No systematic trace element difference between Py3c and Py3a-3b is present (Table 2; Fig. 11e), even though Py3c features pyrite grains and aggregates that are homogeneous in size and have a strong Au–As association (Fig. 10e).

Py3d is marked by the lowest Co (<9.4 ppm) and Ni (<32.5 ppm) contents among all pyrite types (Fig. 10). Compared to Py1 and Py2, Py3d is high in Au (up to 42.2 ppm) and Cu (up to 244 ppm) but low in W (<0.43 ppm), Bi (<0.75 ppm), Pb (<19.2 ppm), and Ti (<109 ppm) (Table 2; Fig. 10). The median As content of Py3d (11604 ppm) is higher than that of Py1 (88.5 ppm) and Py2 (3836 ppm) (Fig. 10). Generally, Py3d has lower contents of most trace elements than Py3a-3c. Similar to Py3a-3c, Py3d also has a strong Bi–Pb–Sb–Ag association. Gold in Py3d is strongly coupled with As–Cu–Se (Fig. 11f).

Compared with Py1, Py4 has higher Au (0.83–6.23 ppm), As (4682–13074 ppm), Cu (9.27–59.0 ppm) and Ti (455–1710 ppm) contents. The As and Cu contents of Py4 are lower than those of Py2, and Py3, whereas the Au content of Py4 is higher than that of Py2 but lower than that of Py3. As shown in Fig. 11g, gold in Py4 is strongly associated with As.

Table 1
Summary of common textures and formation timing for major pyrite types from the Ashawayi gold deposit.

Pyrite type	Textures	Stage	Evidence for timing
Py1	Framboidal and fine-grained euhedral	Pre-ore	Typical framboidal texture, framboids with diameter > 11 μm and cubic shapes similar to diagenetic pyrite
Py2	Medium-grained subhedral to euhedral core	Early ore	Intimately related to Py1; some retain Py1 cubic shape; overgrown by Py3
Py3a-c	Coarse-grained anhedral to subhedral aggregates with micro-inclusions	Main ore	Overgrows Py2; quartz recrystallized as pressure shadows; associated with arsenopyrite, stibnite and chalcopyrite; parallel to early cleavage or disseminated in host rocks
Py3d	Coarse-grained subhedral-euhedral with few sulfide inclusions	Main ore	Crosscut porous Py3c; parallel to the late cleavage in the host rocks, no adjacent quartz-rich pressure shadow
Py4	Relict of preexisting hydrothermal pyrite	Late ore	In supergene yellow ores

Various elements can be incorporated into pyrite from hydrothermal fluids and occur as solid solutions or micro/nanoinclusions (e.g., Thomas et al., 2011; Román et al., 2019; Chinnasamy et al., 2021). For example, Na-, Al-, Mg-, Ca- and Si-bearing microinclusions are observed in the LA–ICP-MS time-resolved profile (Fig. S1a), possibly due to the occurrence of carbonate and silicate inclusions in pyrite. As shown in Fig. 12a, all data plot below the Au solubility line (Reich et al., 2005), and the low Au/As molar ratios (<0.02) suggest that Au occurs mainly as a substituting cation in the crystal structure and that pyrite forms from Au-undersaturated fluids. Furthermore, Au spikes in pyrite are not revealed by LA–ICP-MS measurements (Fig. S1b). This, together with the narrow range of Au contents in the same type of pyrite from the same sample (Table 2), implies that Au occurs mainly as a solid solution (Au^{+}) in pyrite. Copper in the Ashawayi pyrite (up to 1267 ppm) occurs in two forms, as revealed by reflected-light microscopy and LA–ICP-MS time-resolved signal profiles (Fig. 8d and S1b-d): (i) structurally bound Cu and (ii) Cu-bearing microinclusions, including mainly chalcopyrite and minor Zn-Ag–Sb–Cu-bearing minerals (Fig. S1c). Structurally bound Cu is displayed in the LA–ICP-MS depth profile as a flat and smooth ^{63}Cu signal (Fig. S1b). The negative correlations and trends between Cu and Fe in all five types of pyrite (Fig. 11) indicate that substitution between Fe^{2+} and Cu^{2+} is the most likely mechanism for Cu incorporation into the pyrite structure. The lead content in the pyrite is moderately high (up to 558 ppm), and LA–ICP-MS depth profiles show that Pb occurs occasionally as Pb-bearing inclusions in all pyrite groups. The Bi, Sb and Pb in pyrite show clear correlations with each other, suggesting that they may occur as Bi–Pb–Sb micro/nanoinclusions in pyrite, as also evidenced by the coinciding ^{121}Sb, ^{208}Pb and ^{209}Bi peaks in the LA–ICP-MS depth profile (Fig. S1d).

7. Discussion

7.1. Pyrite genesis

On the basis of petrographic observations, pyrite is divided into four types according to morphological characteristics and overgrowth relationships. Geochemical data further strengthen these distinctions and indicate that Py1, and Py2, Py3, Py4 pyrite were formed under different geochemical conditions, i.e., diagenetic and hydrothermal, respectively. Generally, pyrite framboids can be divided into syngenetic and diagenetic framboids, which were deposited in the water column and pore water, respectively (Raiswell and Berner, 1985). Compared with syngenetic framboids, diagenetic framboids are larger (diameter > 11 μm) (Rickard, 2019). Furthermore, euhedral pyrite deposited in sediments is usually thought to be of diagenetic origin (Large, et al., 2007; Taylor and Macquaker, 2011). Therefore, the framboids and euhedral pyrite (Py1) in this study may be diagenetic. In addition, diagenetic pyrite has distinctive trace element ratios of 0.1 < As/Ni < 10, Bi/Au > 1, and Sb/Au > 100 (Gregory et al., 2015). For our samples, Py1 has median As/Ni (0.34), Bi/Au (12.9), and Sb/Au (149) ratios that are within the diagenetic pyrite ranges. Py3 and Py4 have significantly higher median As/Ni ratios (>34.3) but lower Sb/Au (<12.5) and Bi/Au (<1, except for two samples) ratios than Py1 (Table 3), indicating that these pyrites are not sedimentary/diagenetic but rather are hydrothermal. Py2 is transitional between Py1 and Py3 and has diagenetic pyrite-like As/Ni (2.96) and Bi/Au (11.7) ratios but hydrothermal pyrite-like low Sb/Au ratios (47.3). On the binary Au vs As and As/Ag vs Sb/Bi plots (Fig. 12), Py1 data plot in the diagenetic pyrite field (Fig. 12a), while most Py3 and Py4 data plot in the hydrothermal pyrite field (Fig. 12b). Moreover, the Py2 data plot between the Py1 and Py3–Py4 fields (Fig. 12).

Based on the above discussion, it is suggested that the Ashawayi pyrite was formed in different environments. To further discriminate the Ashawayi pyrite classes and their genetic relationships, hierarchical cluster analysis (HCA) was conducted. Generally, selecting useful source-related parameters (instead of using all available parameters) is important for HCA (Peters et al., 2000, 2007; Hao et al., 2009). Nickel-related elemental ratios (e.g., Co/Ni, Zn/Ni, and As/Ni) are often used to determine the pyrite origin (hydrothermal vs syngenetic/diagenetic; Bajwah et al., 1987; Gregory et al., 2015; Ulrich et al., 2011) because they are not strongly affected by metamorphism or hydrothermal overprinting (Large et al., 2007). Furthermore, gold-related elemental ratios are useful, although probably less robust than Ni ratios because the Au content is often near or below the detection limit. However, pyrite in different geochemical environments often contains Au that shows distinctly different trace metal/Au ratios (Me/Au) (Large et al., 2007, 2009,2011; Thomas et al., 2011; Deditius et al., 2014). Therefore, the Sb/Au, Bi/Au, Se/Au, Co/Ni and Zn/Ni ratios were chosen for the HCA (Table 3). One sample (ZK1602-3B in Table 3) lacks Zn/Ni parameters due to its very low Zn content (bdl) but was still included in the HCA by assigning the Zn content to half of the detection limit.

Fig. 13 shows the dendrogram using the Euclidean distance and between-group linkage method by IBM SPSS Statistics. HCA discriminates the analyzed pyrite samples into three classes. Class A pyrite (Fig. 13) is characterized by relatively high Sb/Au, Bi/Au and Se/Au ratios but low Co/Ni and Zn/Ni ratios, and all data plot within the diagenetic pyrite field (Fig. 12a), suggesting a sedimentary formation environment. Class B pyrite has a relatively high Co/Ni ratio and intermediate Sb/Au, Bi/Au, Se/Au, and Zn/Ni ratios between classes A and C (Table 3) and plots in the diagenetic and hydrothermal pyrite fields (Fig. 12). Therefore, class B pyrite was likely formed by hydrothermal reworking of diagenetic pyrite but shows more hydrothermal characteristics, as revealed by class B and class C clustering into a group (Fig. 13). Class C pyrite has the lowest Sb/Au, Bi/Au and Se/Au ratios but more varying Co/Ni and Zn/Ni ratios than classes A and B (Table 3) and plots in the hydrothermal pyrite field (Fig. 12b). Therefore, class C pyrite is also hydrothermal. Hence, the HCA results support petrographic observations and available geochemical data.

7.2. Source of Au and other trace elements

Sedimentary pyrite can effectively release gold and arsenic during greenschist-facies or higher-grade metamorphism of sedimentary rocks and could play an important role during mineralization of some orogenic Au deposits (Pitcairn et al., 2006; Large et al., 2009; Wilson et al., 2013). Synsedimentary and diagenetic pyrites in the host rocks have been reported to provide Au and As for these orogenic Au deposits, such as the Sukhoi Log deposit in Russia and the Bendigo deposit in

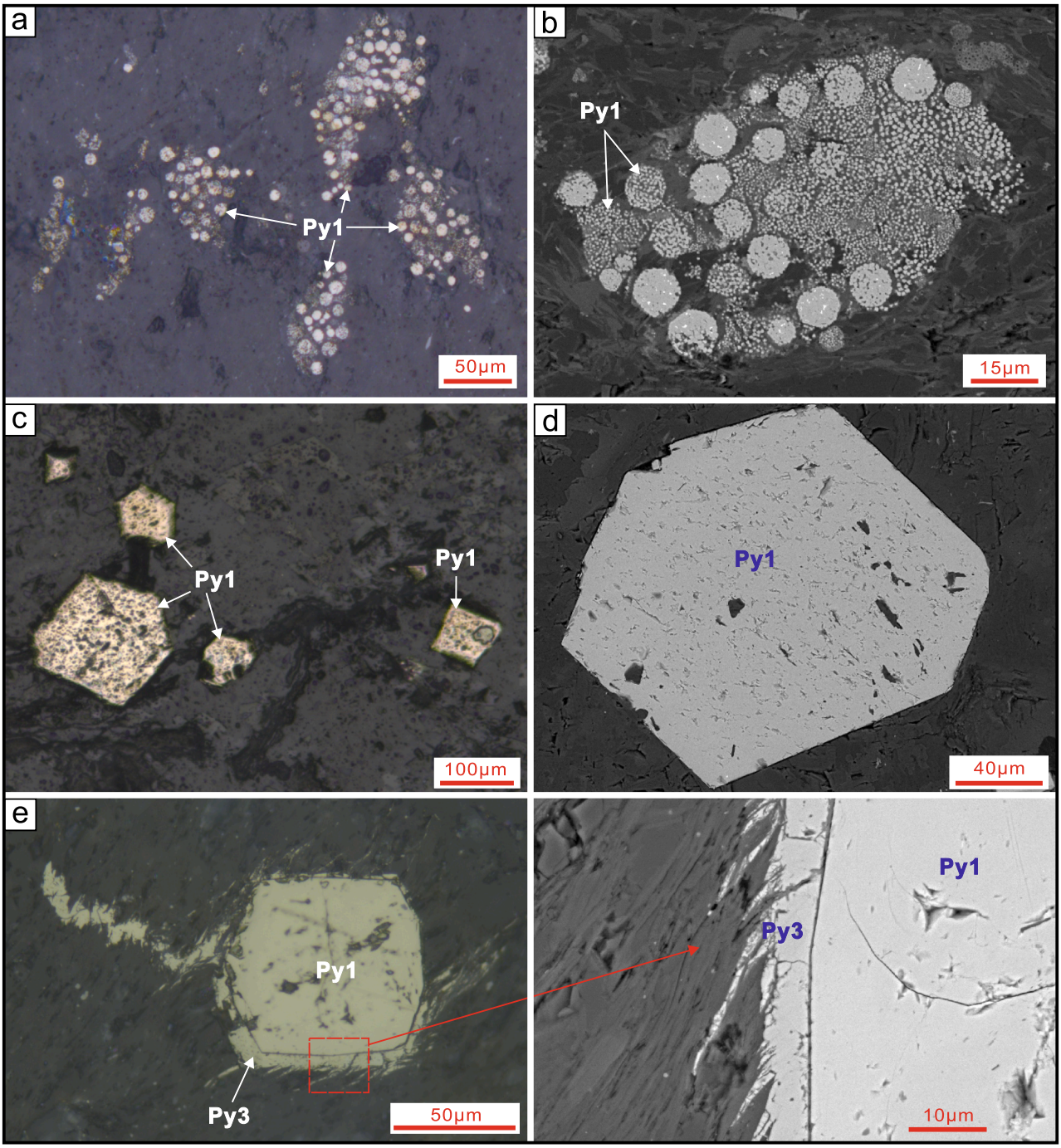

Fig. 6. Textural features of diagenetic preore pyrite (Py1). a. Reflected-light image of Py1a clusters in phyllite; b. backscattered electron (BSE) image of Py1a framboids/clusters in phyllite; c. reflected light image of randomly distributed Py1b in phyllite; d. BSE image of Py1b, showing a homogeneous composition; e. subhedral Py1 overgrown by Py3.

Australia (Large et al., 2011). However, some researchers have suggested that gold in orogenic Au deposits is not derived from precursor sedimentary pyrite and comes from hydrothermal fluid (Li et al., 2020b). Accordingly, it is important to know whether Py1 provided Au in the Ashawayi deposit. The key to resolving this problem is to determine the Au concentrations of Py1 to Py3. The Au concentration in Py1 is lower than 0.34 ppm (median of 0.10 ppm), which is much lower than those in Py2 and Py3 (Fig. 10). The Au concentration in Py1 is very low, and hence is unlikely to be the source for the gold in the Ashawayi deposit. It is more likely that the Au was added by external hydrothermal fluids. Similar to gold, As, Cu, Se and Tl show an increasing trend in concentration from Py1 to Py2 to Py3, which supports the hypothesis of hydrothermal fluids adding these trace elements (Fig. 10). Principal component analysis of trace element data shows that *syn*-ore pyrite has no correlation between Au and Ag–Sb–Bi–Pb (Fig. 11b-e) and only a simple positive correlation between Au and As ± Cu in Py2, Py3c and Py3d (Fig. 11b, e, f), which is a common elemental association in metamorphic systems (Kerr et al., 2018). Previous H and O isotope studies have indicated that hydrothermal fluids were mainly metamorphic fluids in the Au mineralization stage (Zhang et al., 2021). According to the inferred fluid source for the hydrothermal fluid and elemental association of pyrite, the Au and As in Py2 and Py3 were most

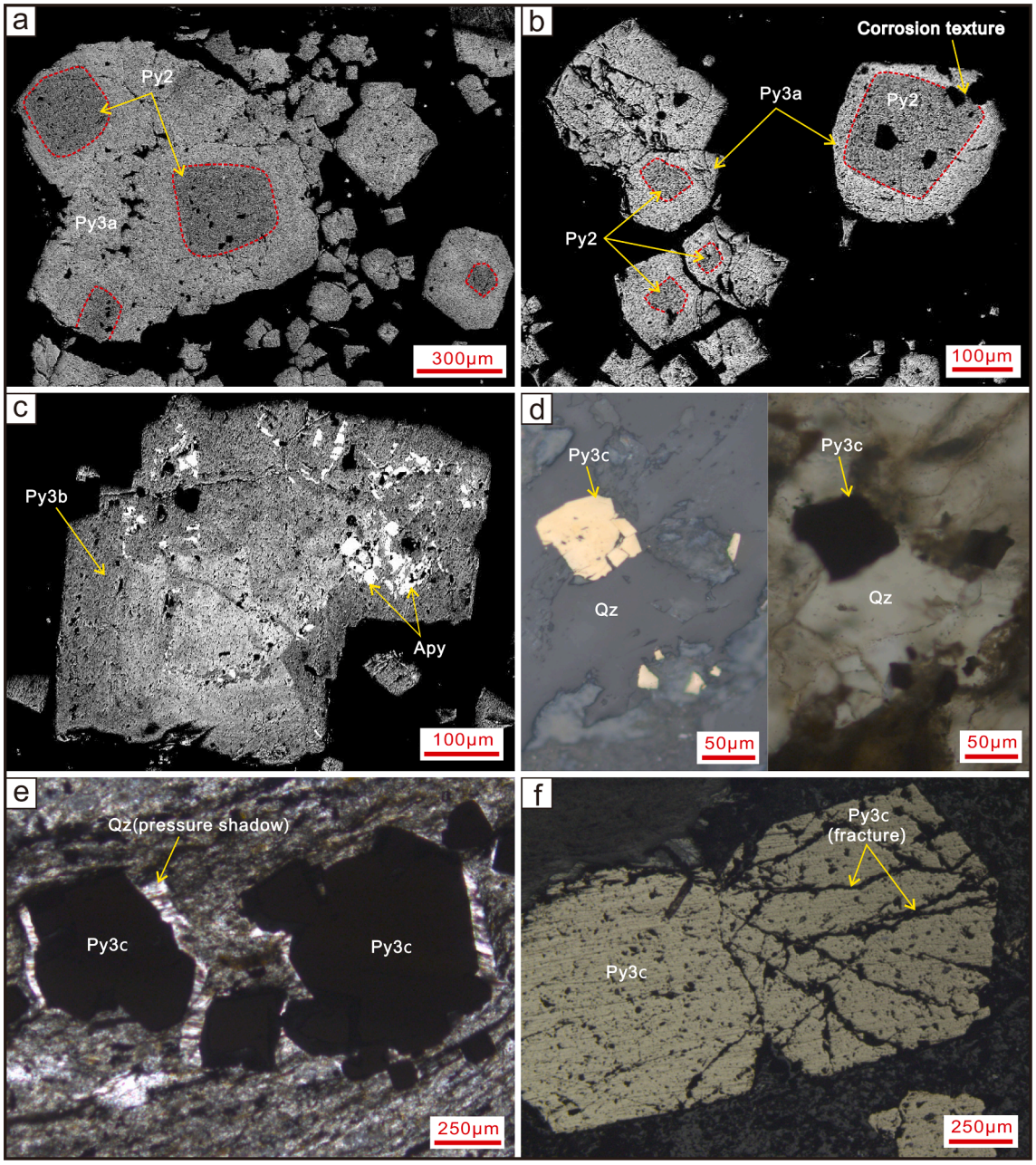

Fig. 7. Textural features of Py2 and its relations to Py3. a. Backscattered electron (BSE) image of subhedral porous Py2 overgrown by porous Py3a rims (with stronger reflectance), indicating higher average atomic mass (Au-/As-rich in this case); b. BSE image of the corrosion texture between porous Py2 and Py3a, indicating no direct overgrowth of Py3a on Py2; c. BSE image of porous Py3b with irregular oscillatory zoning and fine arsenopyrite inclusions; d. reflected light (RL; left) and transmitted light (TL; right) images of subhedral Py3c in a quartz vein; e. TL image of subhedral Py3c surrounded by a quartz pressure shadow; f. RL image of Py3c fractured/deformed by microshearing in phyllite.

likely sourced from metamorphic fluid.

Although it is less likely that Au and As were derived from Py1, other metals from Py1 possibly contributed to the formation of the Ashawayi deposit and are important to evaluate. Co/Ni ratios have long been used to distinguish hydrothermal and syngenetic/diagenetic pyrites (Bralia et al., 1979; Bajwah et al., 1987; Large et al., 2014), and Co/Ni < 1 is usually considered to indicate a sedimentary origin (Bajwah et al., 1987). No significant difference is observed in Co/Ni ratios between Py1 and other types of pyrite, all of which have consistent Co/Ni ratios < 1, except for two spots in Py2 and one spot in Py3 with Co/Ni ratios > 1 (Fig. 12c). These results may indicate that Co and Ni in Py2 and Py3 from the Ashawayi deposit have main contributions from sedimentary origins. Ni concentrations significantly decrease from Py1 (up to 4749 ppm) to Py3 (with a maximum of 32.5 ppm). A similar decrease is observed for Co concentrations from the early to the main Au mineralization stage, i.e., from Py2 to Py3 (Fig. 10), indicating that these elements were mainly sourced from Py1 rather than from the deep metamorphic fluid. This observation is supported by recent findings (Li et al., 2020b) that metamorphic fluids from the metamorphism of sedimentary rocks do not alter low sedimentary Co/Ni ratios.

It is likely that pyrite dissolution–reprecipitation was responsible for metal release from sedimentary pyrite. Such an argument is based on the following evidence: (1) Py2 has diagenetic pyrite-like As/Ni and Bi/Au ratios but a low Sb/Au ratio, similar to that of hydrothermal pyrite (Table 3); (2) many voids occur in some Py1, which most likely were caused by leaching some of the trace elements from Py1 during

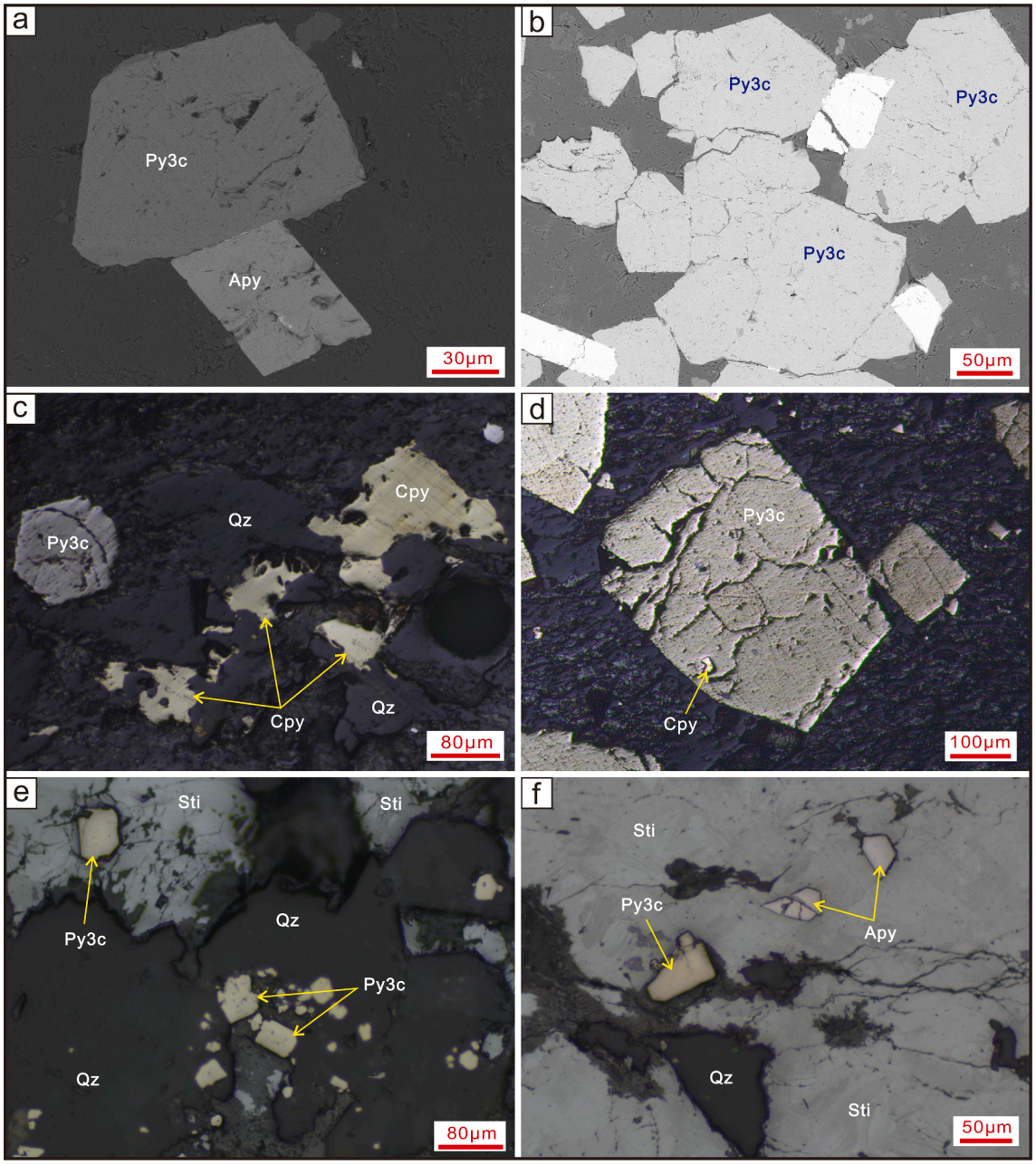

Fig. 8. Textural features of Py3 and its relations to other minerals. a. Backscattered electron (BSE) image of Py3c coexisting with arsenopyrite; b. BSE image of Py3c intergrown with arsenopyrite (Apy); c. reflected light (RL) image of Py3c and chalcopyrite (Cpy) in a quartz vein; d. RL image of fractured Py3c with a chalcopyrite inclusion; e. RL image of Py3c inclusions in stibnite (Sti); f. RL image of Py3c and arsenopyrite inclusions in stibnite.

dissolution–reprecipitation, and some Py2 grains retain Py1 cubic crystals (Fig. 7a, b); and (3) the corroded boundary of Py1 and Py2 is surrounded by Py3 (Fig. 6e, 7b), which is indicative of Py3 crystallization during or after the dissolution of early-formed pyrite. Such a proposition is also supported by the Co and Ni concentrations decreasing from Py1 to Py3; it is expected that dissolution–reprecipitation would result in lower trace element contents in the recrystallized grains (Chinnasamy, et al., 2021; Qiu et al., 2021). For Co, its remobilization under greenschist-facies conditions is related to fluid-mediated dissolution–reprecipitation of early-formed pyrite (Qiu et al., 2021).

Due to the similar ionic radii between Ni and Co, in this case, the relevant reaction for Ni released from sedimentary pyrite is as follows:

$$(Fe, Ni)S_2 + 3Cl^- \rightarrow FeS_2 + NiCl_3^- + H_2S + O_2.$$

This dissolution–reprecipitation process also likely led to the liberation and remobilization of gold and arsenic from the structure of Py1 into the metamorphic fluid. However, given the small pyrite/quartz ratio by mass, partial replacement of Py1 by dissolution–reprecipitation and concentrations of Au and As in Py1 (Au $\leq$ 0.34 ppm, As $\leq$ 239.81 ppm; Table 2), the quantity of gold and arsenic remobilized from Py1 is not sufficient to form economic mineralization. Thus, an increase in Au and As contents in *syn*-ore pyrite is observed, most likely due to the intermittent fluctuation in the fluid composition, which can be attributed to the injection of a new hydrothermal fluid during episodic fault-valve action (Cox et al., 2001).

Based on the discussion above, the sedimentary pyrite (Py1) in the host sedimentary rock (Carboniferous Kalachirga Formation) mainly contributed to the budget of some trace elements, such as Co and Ni; however, the deep metamorphic fluid likely provided Au, As, Cu, Se and Tl to the Ashawayi gold deposit.

Taken together, the Carboniferous sedimentary pyrite from the host

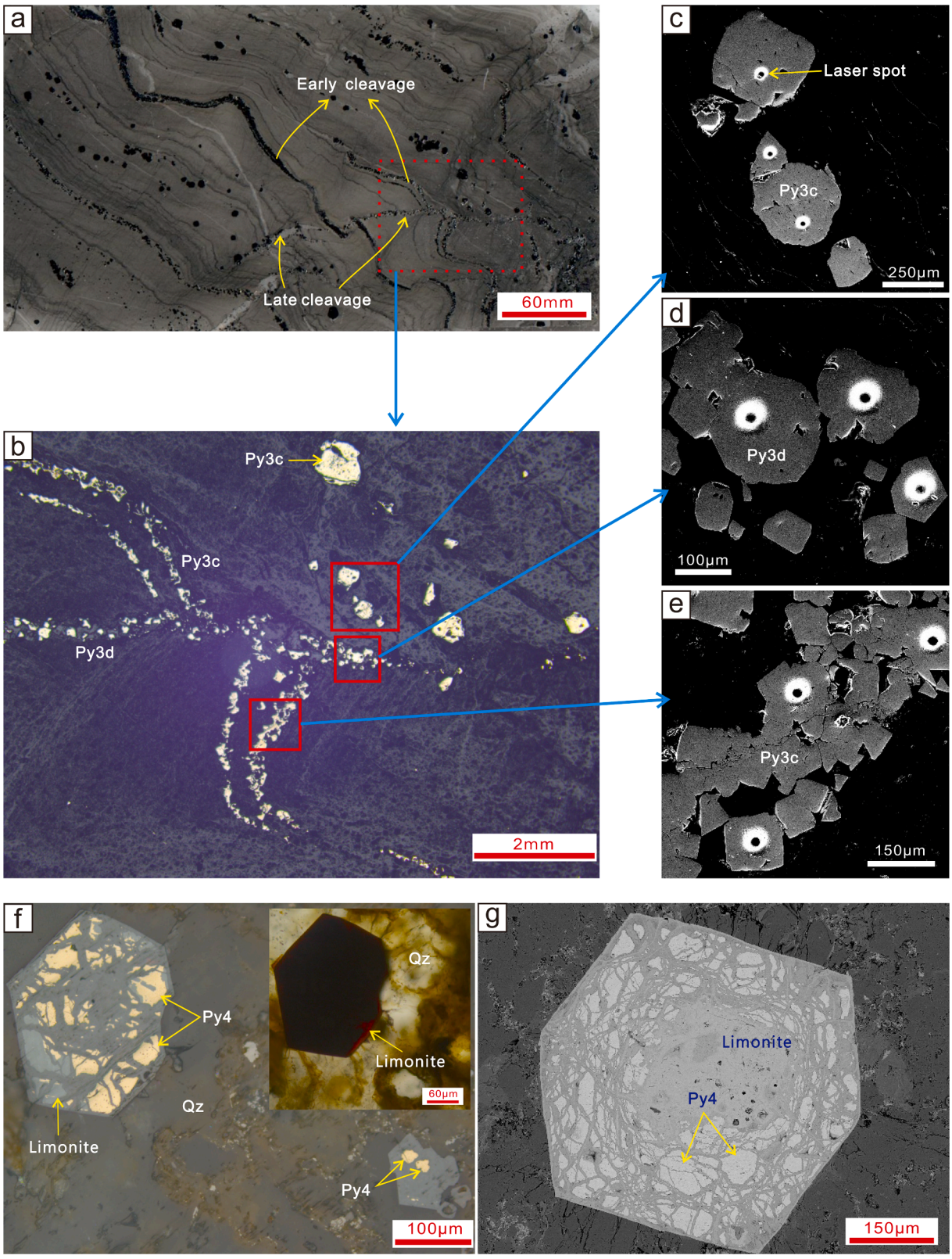

Fig. 9. Textural features of Py3 and Py4. a. Thin section image of Py3c parallel to the early cleavages in phyllite and crosscut by Py3d (which precipitated along late cleavages), suggesting post-tectonic Py3d formation; b. reflected light (RL) image of Py3d crosscutting Py3c and disseminated Py3c; c. backscattered electron (BSE) image of disseminated Py3c; d. BSE image of homogeneous Py3d, with a few pores and fractures; e. BSE image of banded Py3c; f. RL image of Py4 of earlier pyrite relicts in quartz vein; g. BSE image of homogeneous Py4 and limonite in fissures of earlier pyrite.

Table 2
LA–ICP-MS data summary of pyrite from the Ashawayi gold deposit. N.B. Data below the detection limit are assigned to half of the corresponding detection limit to calculate the average and median values.

Pyrite		Mg	Al	Ca	Ti	V	Co	Ni	Cu	Zn	As	Se	Mo	Ag	Sb	W	Au	Tl	Pb	Bi
Pre-ore stage (n = 11); Diagenetic pyrite																				
Py1	Median	6.57	10.01	12.04	2361.55	7.95	59.65	341.09	7.79	3.20	88.45	2.45	0.06	0.04	16.50	3.91	0.10	0.01	18.49	1.05
	Ave	9.14	15.09	32.13	2481.32	9.69	72.06	772.78	7.29	3.53	104.47	2.66	0.61	0.06	14.26	3.98	0.11	0.02	17.90	1.29
	Min	1.95	4.18	bdl	6.25	0.17	17.46	144.44	1.37	2.40	49.40	bdl	bdl	bdl	0.34	0.00	bdl	bdl	2.63	0.08
	Max	34.76	42.98	92.37	4191.40	26.17	225.03	4749.18	13.22	5.77	239.81	6.18	6.05	0.18	24.70	11.32	0.34	0.04	31.23	3.06
Early ore stage (n = 7); Pyrite showing intermediate features between diagenetic and hydrothermal origin																				
Py2	Median	14.76	285.88	38.68	568.45	2.21	215.33	732.89	18.02	4.03	3836.18	6.52	0.06	0.26	23.99	1.06	0.61	0.05	63.79	6.15
	Ave	45.06	485.73	60.88	792.30	2.47	684.49	1019.17	31.73	4.57	10541.56	7.62	0.08	0.26	21.99	1.27	1.55	0.07	59.84	8.87
	Min	2.07	34.01	bdl	26.69	0.27	0.51	3.77	9.35	2.14	35.49	3.98	bdl	0.09	0.85	0.11	0.02	bdl	5.09	0.56
	Max	152.92	1945.53	234.46	1787.99	5.88	3041.40	2854.88	81.01	6.59	31006.10	12.45	0.25	0.45	40.87	3.92	4.22	0.14	104.94	18.78
Main ore stage (n = 77); Hydrothermal pyrite; Py3a occurs as rims on Py2, while Py3b and Py3c with oscillatory compositional zonation and without zoning, respectively; Py3d crosscuts Py3c																				
Py3a	Median	3.81	24.59	21.68	882.44	2.67	11.54	66.47	58.60	2.26	26067.93	4.80	0.07	0.14	16.08	4.16	12.21	0.08	23.21	1.65
	Ave	4.66	38.75	19.92	928.18	3.32	38.61	303.94	61.19	2.41	26709.45	4.61	0.32	0.19	21.42	5.05	13.44	0.10	30.66	1.68
	Min	0.80	4.70	bdl	87.93	0.10	2.56	21.60	39.12	1.51	20497.40	1.21	bdl	0.08	2.28	0.42	2.94	bdl	5.79	0.36
	Max	10.51	134.08	27.86	2048.78	7.25	246.14	2185.47	85.64	3.69	35337.02	7.78	2.13	0.43	54.21	12.15	26.36	0.48	65.04	3.20
Py3b	Median	9.05	4.25	59.67	15.93	0.16	38.11	158.94	344.87	2.98	38070.23	16.23	0.28	0.42	24.82	0.42	61.75	0.21	26.75	1.40
	Ave	21.79	149.41	67.04	673.43	2.81	39.67	175.70	364.11	2.96	39849.62	15.64	2.38	0.73	41.19	5.50	62.26	0.24	48.22	1.84
	Min	1.80	1.18	bdl	7.95	bdl	2.62	36.17	125.60	1.73	23872.73	10.75	0.06	0.17	6.43	0.06	17.67	0.05	11.77	0.47
	Max	97.16	1130.34	222.78	3790.16	14.20	93.28	353.05	617.12	4.42	65182.07	18.84	11.55	2.07	86.06	28.39	106.83	0.49	100.43	4.56
Py3c	Median	4.06	14.27	28.29	840.38	2.73	18.62	97.42	59.74	2.63	18818.26	6.17	0.00	0.25	17.08	4.15	8.36	0.09	28.87	2.13
	Ave	14.75	128.34	42.66	886.95	3.04	34.45	141.36	144.35	4.79	21983.38	7.83	0.13	0.53	36.86	5.52	16.89	0.13	58.57	4.02
	Min	bdl	bdl	bdl	5.55	bdl	0.16	3.36	5.07	bdl	5973.15	bdl	bdl	bdl	1.98	bdl	0.32	bdl	4.04	0.16
	Max	410.51	3662.52	583.56	2812.65	16.27	166.70	575.40	1082.16	79.32	37207.01	21.25	2.45	4.88	221.59	44.16	102.72	0.87	557.85	18.82
Py3d	Median	6.88	2.30	13.48	21.49	0.11	3.04	14.38	113.20	3.27	11604.89	10.40	0.10	0.05	2.79	0.10	22.40	0.04	2.81	0.20
	Ave	70.34	2.72	16.41	35.41	1.78	3.92	17.58	111.08	3.99	12639.92	10.31	0.13	0.08	4.76	0.16	22.43	0.04	5.27	0.32
	Min	1.25	bdl	bdl	9.19	bdl	0.75	10.19	3.70	2.27	1723.11	6.50	bdl	bdl	0.73	bdl	0.34	bdl	0.73	0.14
	Max	391.77	5.92	34.85	108.99	0.12	9.40	32.54	244.15	8.05	21471.55	13.68	0.23	0.21	16.13	0.43	42.16	0.07	19.20	0.75
Late ore stage (n = 9); Hydrothermal pyrite; Relict of preexisting pyrite in the oxidized ores																				
Py4	Median	3.58	20.41	41.77	911.69	1.73	47.19	221.39	17.14	3.38	7362.97	5.63	0.08	0.05	8.97	3.14	1.68	0.04	14.04	1.54
	Ave	8.68	19.14	93.49	927.90	2.49	56.29	237.42	23.22	4.72	7949.89	5.68	0.30	0.14	8.75	3.05	2.26	0.05	13.42	1.87
	Min	1.10	3.46	bdl	455.28	1.04	12.80	46.24	9.27	1.74	4682.37	3.16	bdl	bdl	bdl	1.51	0.83	0.03	8.03	1.19
	Max	35.32	48.49	497.67	1709.70	6.15	117.15	427.84	59.01	12.11	13074.30	8.03	1.53	0.84	0.04	5.48	6.23	0.09	17.70	3.63

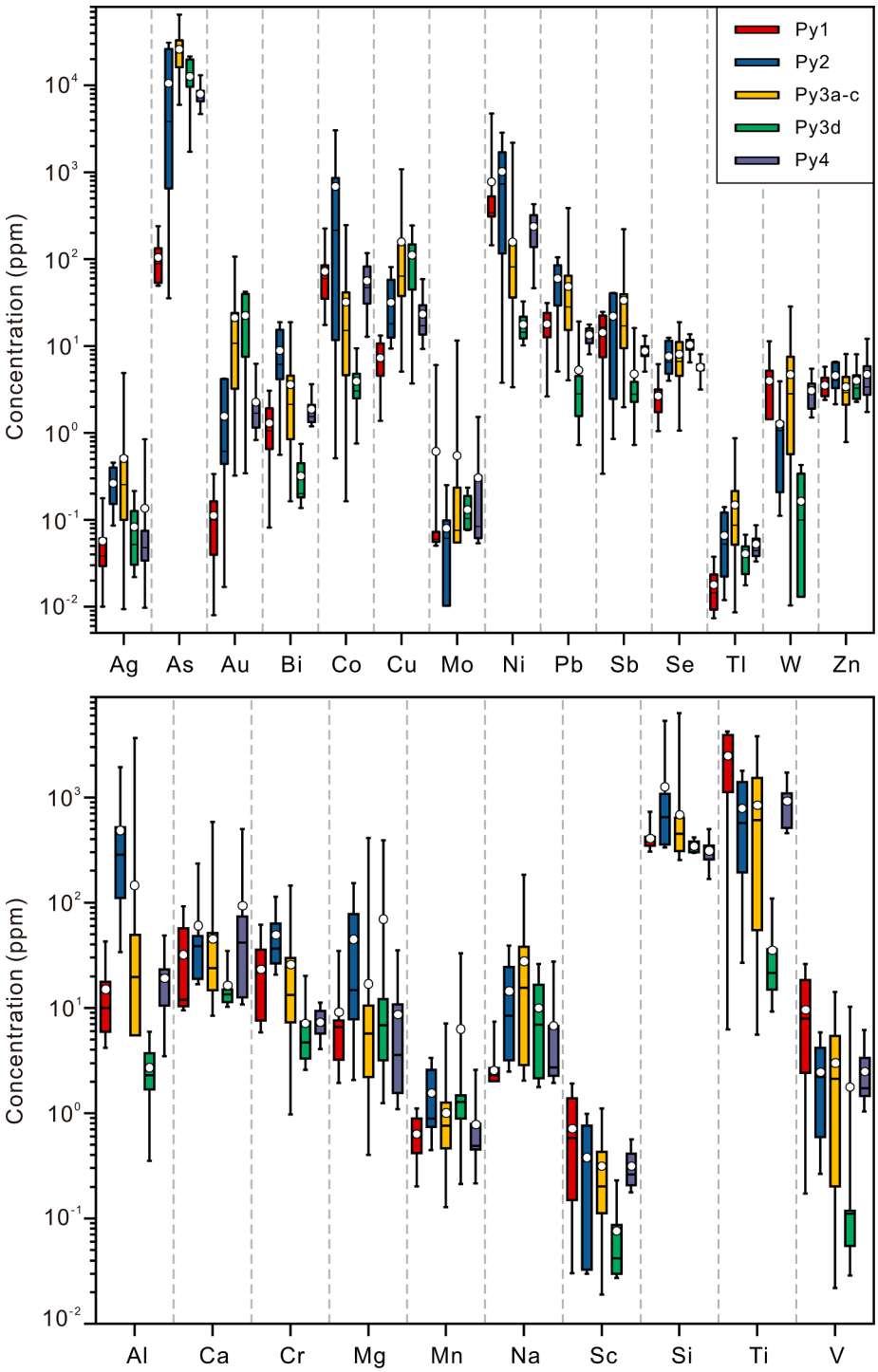

Fig. 10. Box and whisker plots of trace elements for the different pyrite generations in the Ashawayi deposit. Boxes outline the 25th to 75th percentiles, and whiskers extend to the minimum and maximum values. Median and mean values are shown as solid black lines and white circles, respectively. Data below the detection limit are assigned to half of the corresponding detection limit.

rock was not the main source of Au during economic mineralization in the Ashawayi deposit. However, as the Au contents of pyrite in other sedimentary rocks of the southwestern Tianshan orogen have not yet been reported, we cannot confirm which sedimentary rocks may have had the potential to contribute some Au and As to the Ashawayi deposit during regional metamorphism.

7.3. Pyrite evolution and mechanisms of ore precipitation

Py1 is characterized by low Au (median of 0.10 ppm, except for one analysis that falls below the detection limit) and As (median of 88.5 ppm), together with a median Co/Ni ratio of 0.15, which is comparable to that of diagenetic pyrite from the Qiuling orogenic gold deposit in the Qinling orogen, where deposition occurred in a sulfate-limited environment (Li et al., 2020b). Median contents of Ni (341 ppm) and Co (59.7 ppm) in Py1 from the Kalachirga Formation carbonaceous phyllite

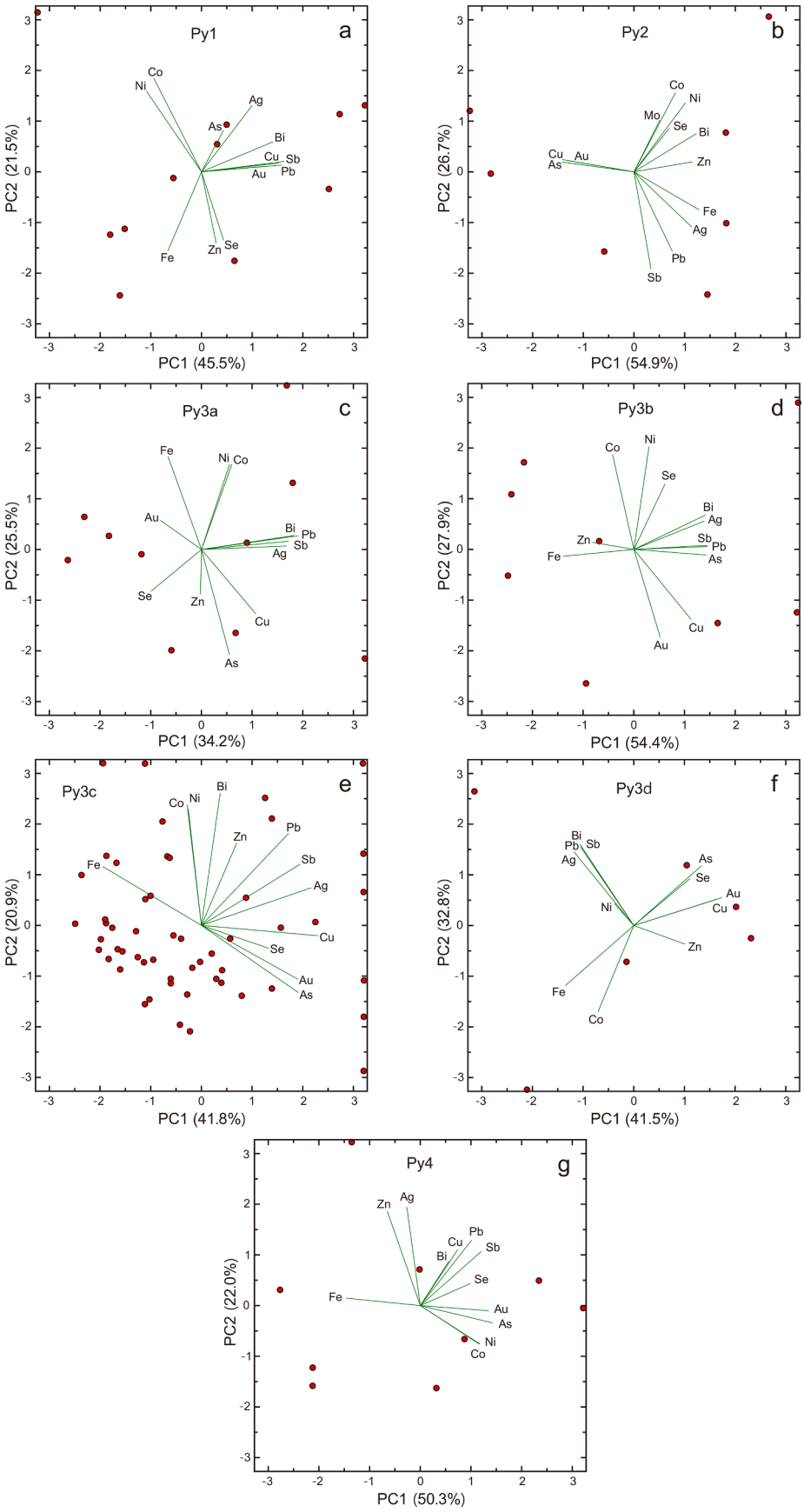

Fig. 11. Biplots for varimax-rotated principal component analysis (PCA) of different pyrite generations at Ashawayi.

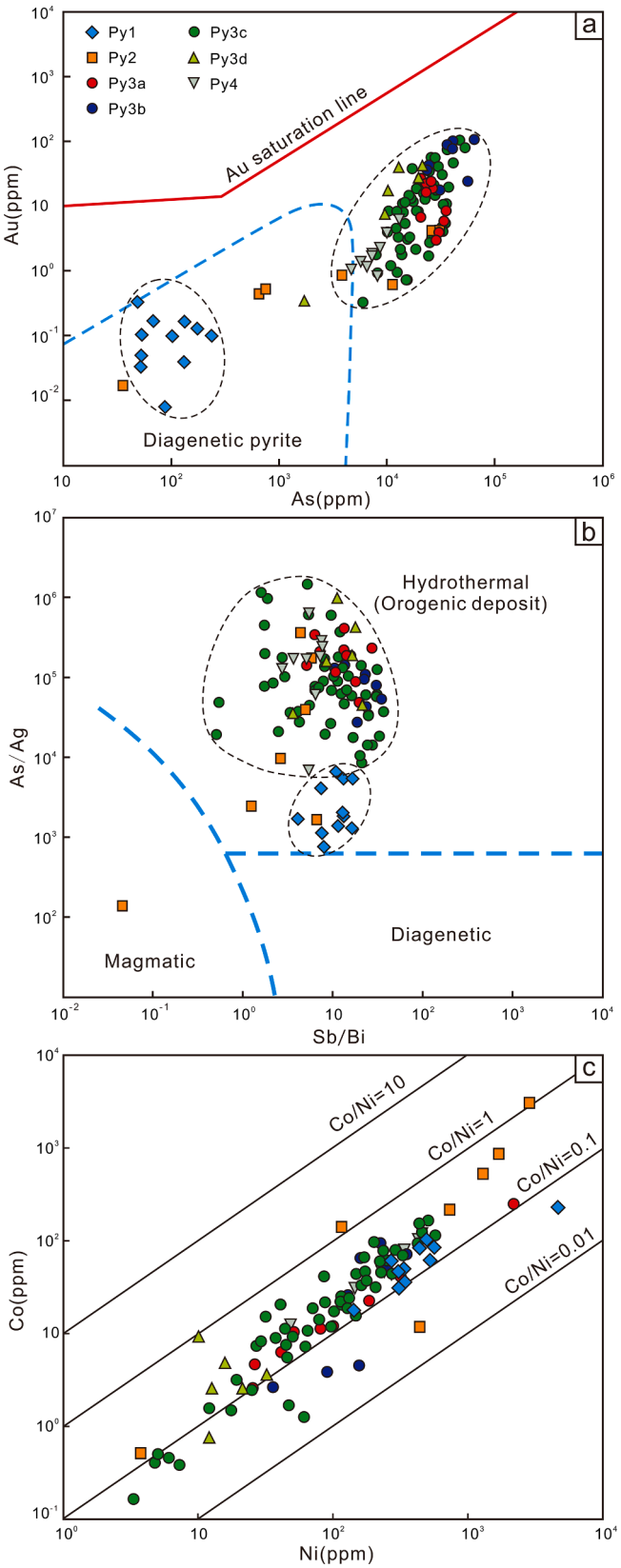

Fig. 12. Binary plots of Au vs As (a), Sb/Bi vs As/Ag (b), and Co vs Ni (c) for the different pyrite types in the Ashawayi deposit. Base maps a and b are from Large et al. (2011) and Augustin and Gaboury (2019), respectively. All Py1 data plot in one area, while Py3 and Py4 plot in another area, and the Py2 data plot between these two areas in Figures a and b. Most data points (except for four) have Co/Ni < 1.

and sandstone are lower than those of Hamersley Basin sedimentary pyrites (median values of 813 ppm Ni and 465 ppm Co), and the median Mo content (0.06 ppm) is also lower than that in the Kapai Slate sedimentary pyrite (1.91 ppm), which was deposited under anoxic to euxinic conditions (Gregory et al., 2016). Hence, Py1 was formed by diagenesis in an anoxic to euxinic environment.

After Py1 formation, Py2 formed at the first introduction of the hydrothermal fluid and may have reacted with Py1, presumably during the early phase of shearing. As previously mentioned, Py2 has geochemical features of both sedimentary and hydrothermal pyrites, and some of them retain Py1 cubic crystals (Fig. 7a, b), suggesting hydrothermal overprinting (Table 3; Fig. 13). The gold contents of Py2 (0.02–4.22 ppm) are lower than those of Py3 (0.32–107 ppm). A similar trend is also shown for the contents of As and Cu (Fig. 10), which indicates that the early-ore-stage fluid carried low amounts of As, Au and Cu, as reflected by the darker appearance of the core in BSE images (Fig. 7a, b).

Following this early gold introduction episode, the majority of the anhedral to euhedral Py3 with high As, Au and Cu contents, accompanied by many small quartz grains, precipitated during progressive shearing. Since no replacement textures are identified between Py3a, Py3b and Py3c, these pyrite grains may have formed successively or almost simultaneously from an evolving ore fluid. The last sulfide inferred to have formed during this main ore stage is Py3d, which displays a crosscutting relation with Py3c and is depleted in Au, As, Cu, Sb, Co, Ni, W and Pb relative to Py3a–Py3c. Compared with Py3a–Py3c, Py3d has much fewer pores and microfissures (Fig. 9d) and no quartz-rich pressure shadows. We therefore suggest that the low metal contents in Py3d are associated with its late precipitation, likely from the residual ore fluids accompanied by the weakening of shearing motion.

After the formation of Py3, abundant oxidized and cool meteoric water incursion may have occurred in the metallogenic system, as supported by H—O isotope data (Zhang et al., 2021), and consequently caused the gradual oxidation of former pyrite and the formation of Py4 and limonite (Fig. 9f, g). Py4 shares similar chemical features with Py3, suggesting that Py4 originated from hydrothermal pyrite but not diagenetic pyrite, as supported by Py4 and Py3 clustering into a class based on hierarchical cluster analysis (Fig. 13). Therefore, Py4 is the relict of Py3 and has lower contents of ore-forming materials (such as Au, As, and Cu) than Py3 (Fig. 10), which is likely associated with leaching of Py3 during gradual oxidation.

Fluid boiling and phase separation can be inferred to occur in hydrothermal systems based on pyrite textures and trace element distributions, as described by Li et al. (2018) and Román et al. (2019). In the Ashawayi deposit, Py3a-3c pyrite grains display zones with porous textures and abundant mineral micro- to nanoinclusions (mainly arsenopyrite and chalcopyrite) (Figs. 7, 8), with the development of oscillatory zoning in Py3b (Fig. 7c), suggesting rapid metal deposition under boiling. Additionally, Py3a and Py3b display negative to weakly positive correlations between Au and As, respectively (Fig. 11c, d), which are caused by rapid pyrite crystallization (Fougerouse et al., 2016). Recent experimental results show that decoupling of Au and As occurred at the colloform mantles of cement pyrite from the Daqiao orogenic Au deposit, central China; this is attributed to mantle formation related to rapid disequilibrium precipitation from a highly FeS_2-supersaturated fluid, where Au incorporation into pyrite was controlled mostly by lattice defects produced by rapid nucleation (Wu et al., 2021). As reported by Zhang et al. (2021), the existence of three different fluid inclusions in the main-stage quartz in the Ashawayi deposit and their divergent homogenization behaviors at very similar temperatures also indicate that fluid boiling rapidly discharged their transported elements due to decreasing pressure. Thus, we infer that Au and As are decoupled in pyrite in the Ashawayi deposit, most likely due to rapid pyrite crystallization, which can be attributed to depressurization-induced fluid boiling.

However, some examples show irregular contact boundaries between Py1 and Py3 (Fig. 6e) and the existence of hydrothermal minerals

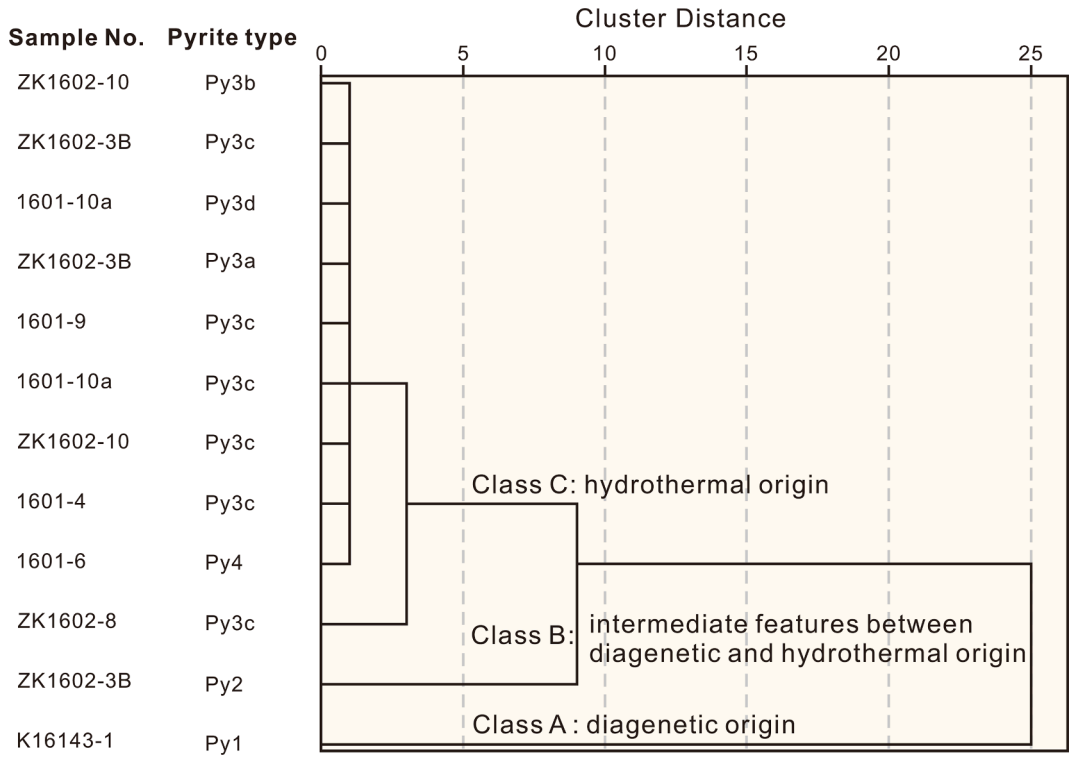

Fig. 13. Hierarchical cluster analysis results for the pyrite classes in the Ashawayi deposit. Py2 shows more hydrothermal fluid influence, as revealed by Py2 and Py3 clustering into a group, while Py4 implies a hydrothermal origin.

Table 3
Trace element ratios used in hierarchical cluster analysis for pyrite from the Ashawayi gold deposit. N.B. Trace element ratios assigned by the median values in pyrite for every sample.

Sample no.	Pyrite	Sb/Au	Bi/Au	Se/Au	Co/Ni	Zn/Ni
K16143-1	Py1	149.31	12.86	19.97	0.15	0.01
ZK1602-3B	Py2	47.32	11.75	12.15	0.40	0.00
ZK1602-3B	Py3a	2.10	0.13	0.40	0.13	0.03
ZK1602-10	Py3b	0.55	0.02	0.27	0.20	0.02
ZK1602-3B	Py3c	0.65	0.06	0.40	0.11	0.10
ZK1602-8	Py3c	12.49	10.31	8.89	0.31	0.07
1601–4	Py3c	4.89	2.38	2.75	0.22	0.02
1601–9	Py3c	1.66	0.18	0.43	0.20	0.01
1601-10a	Py3c	2.23	0.25	0.82	0.25	0.02
ZK1602-10	Py3c	2.93	0.14	0.24	0.08	0.10
1601-10a	Py3d	0.14	0.01	0.53	0.16	0.29
1601–6	Py4	4.51	0.91	2.98	0.22	0.02

(arsenopyrite, chalcopyrite, quartz, and calcite) in Py1, suggesting the interaction between fluid and sedimentary pyrite. Furthermore, the decreasing trend in the concentrations of Co and Ni from Py1 to Py3 (Fig. 10) indicates that Py1 may have contributed some of these trace elements to Py2 and Py3. The contribution of trace elements cannot occur if there is no interaction between Py1 and the ore-forming fluid. The cogenetic pyrite and arsenopyrite, chalcopyrite, and hydrothermal calcite in the sedimentary rocks (Fig. 6h, 8a-c) suggest that the ore fluids also reacted with the Fe carbonate in the sedimentary rocks. Fluid – wallrock/mineral interactions have been documented in many orogenic-type gold deposits, such as the Golden Mile deposit in Western Australia (Evans, et al., 2006), Qiuling deposit in China (Li et al., 2020b), and Chan'an deposit in SW China (Yang et al., 2021).

7.4. Metallogenic type of the Ashawayi gold deposit

Recently, supervised machine learning methods, such as random forests and artificial neural networks (ANNs), have been used to indicate ore deposit types based on pyrite geochemical data (Gregory et al., 2019; Zhong et al., 2021). We applied LA–ICP-MS pyrite trace element data with the assistance of a trained ANN-based classifier by Zhong et al. (2021) to determine the genesis of the Ashawayi deposit. The trained algorithms show that many Py2, Py3, and Py4 pyrite samples have affinities to those of orogenic deposits worldwide (71.4 %, 90.9 % and 66.7 % for Py2, Py3, and Py4, respectively, Fig. 14; Table S2). This result is also consistent with geological and geochemical observations. The orebodies in the Ashawayi deposit are strictly controlled by ductile–-brittle shear zones and faults. The mineralization styles are dominated by auriferous quartz veins. The hydrothermal alterations include sulfidization, sericitization, silicification, and carbonation. Most of the *syn*-ore pyrite lacks a positive correlation between Au and Ag–Sb–Bi–Pb. The hydrothermal fluid had low salinity, was rich in CO_2 and evolved from a metamorphic to a meteoric origin (Zhang et al., 2021). These features support the interpretation of the Ashawayi deposit as an orogenic gold system (Chen and Fu, 1992; Kerrich et al., 2000; Groves et al., 2003; Hagemann and Luders, 2003; Chen, 2006, 2013; Chen et al., 2012b; Zhou et al., 2014a, b, 2015, 2022; Kerr et al., 2018). The Ashawayi deposit is located between the Sawayaerdun and Bulong deposits. The Sawayaerdun and Bulong deposits are constrained to have formed from 323.9 ± 4.8 to 282 ± 12 Ma through pyrite re-Os dating (Zhang et al., 2017) and at 258 ± 15 Ma through quartz Rb-Sr dating (Zhao et al., 2002), respectively. Quartz from the Ashawayi deposit yields an Rb-Sr isochron age of 257 ± 1.3 Ma (Zhou's unpublished data). These ages strongly suggest that the time of the Ashawayi mineralization is consistent with the time of strike-slip movement that was likely related to postcollisional crustal thinning in the southwestern Tianshan orogen (295–240 Ma; de Boorder, 2012; Huo, 2019; Li et al., 2020a), and it may be best classified as a tectonic regime of postcollisional strike-slip extension rather than the usual compressional to transpression regimes (Groves et al., 1998; Goldfarb et al., 2001, 2005). This argument is supported by the field structural measurements and analysis of conjugate shear joints and mineralized veins in the Ashawayi deposit,

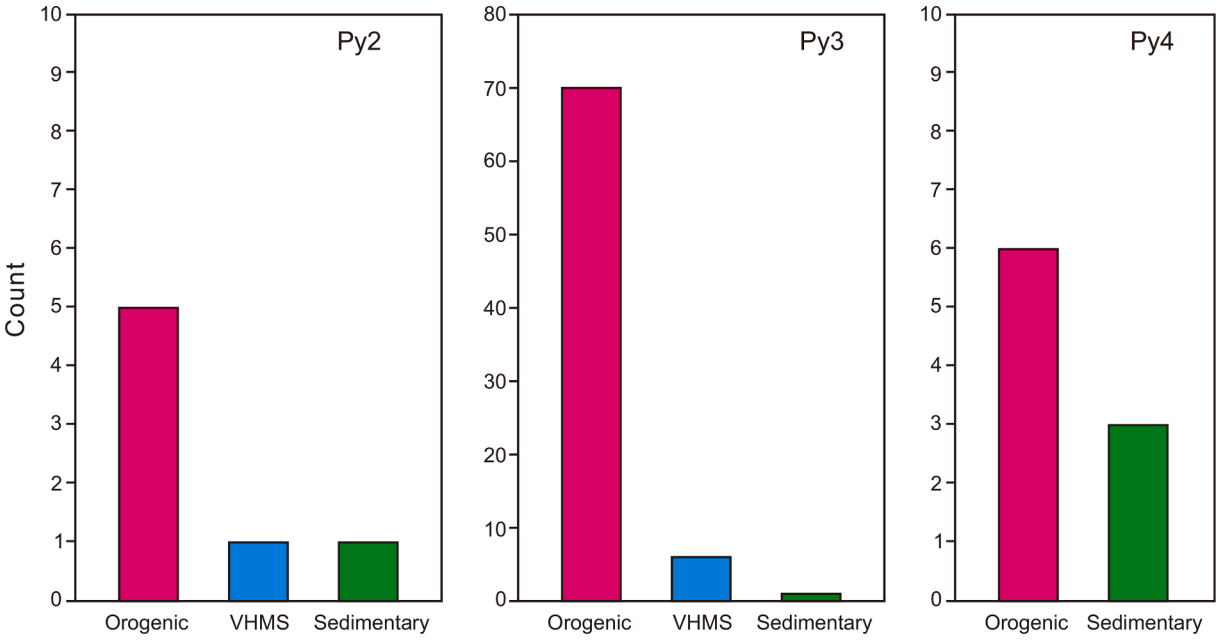

Fig. 14. Histogram of the classification of hydrothermal pyrite generations from the Ashawayi deposit using artificial neural network discrimination algorithms from Zhong et al. (2021). N.B. VHMS, volcanic-hosted massive sulfide deposits.

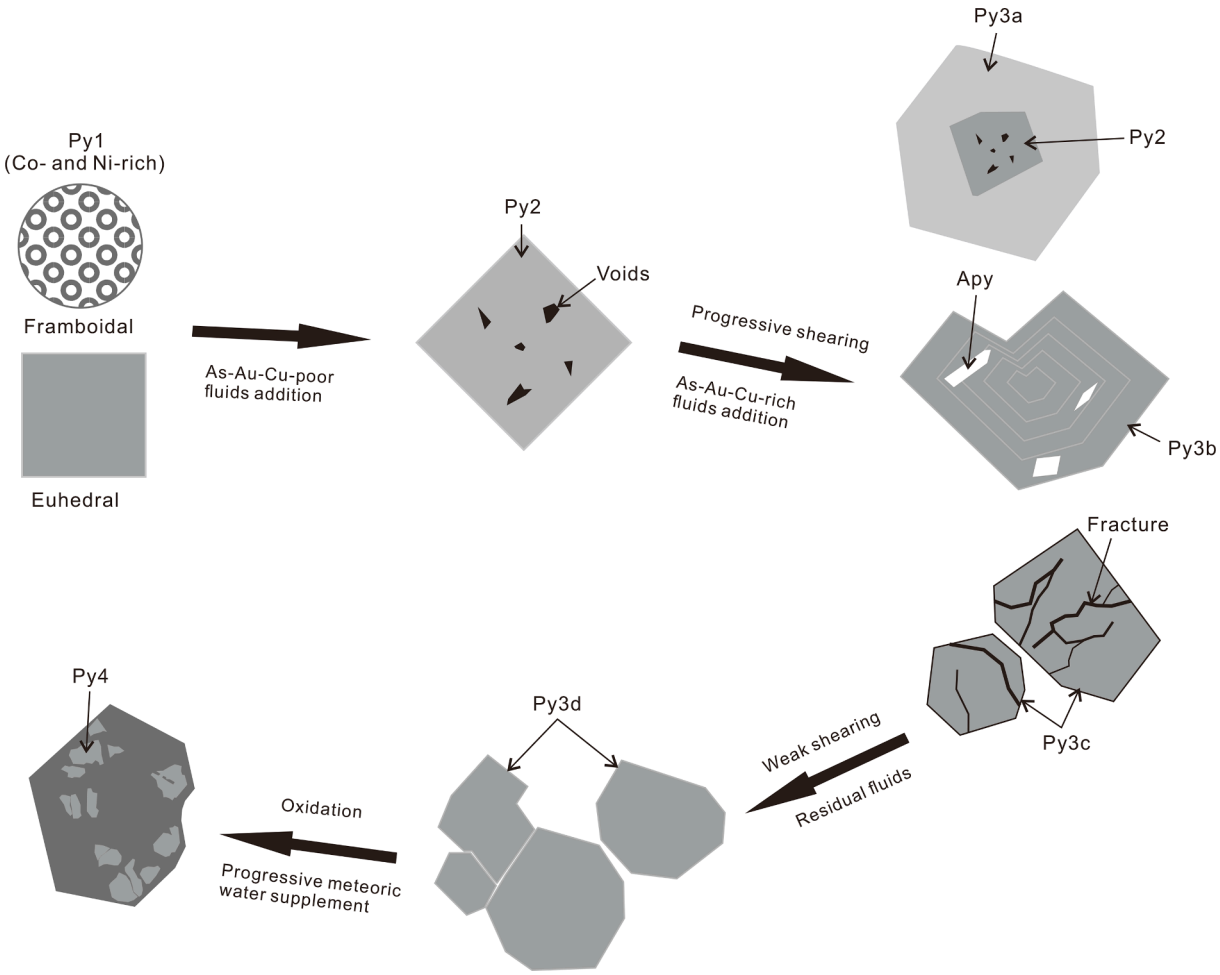

Fig. 15. Schematic model for the formation of different pyrite generations in the Ashawayi gold deposit.

suggesting that the main principal stress in the ore stage was NE–SW-directed, which is consistent with the regional shear direction (Zhou et al., unpublished data). Therefore, it is reasonable to deduce that the Ashawayi deposit was an orogenic-type system formed in association with regional strike-slip deformation and metamorphism during post-collisional crustal thinning.

During the collision between the Tarim and Kazakhstan cratons in the late Paleozoic, the crust was rapidly uplifted and eroded, leading to dextral strike-slip extensional deformation along NE-trending faults. Deep-seated metamorphic ore fluids may have ascended along these faults, decompressed, and then reacted with Py1 in the Kalachirga Formation to generate early-stage Py2 (Fig. 15). During the main ore stage, the fluid system depressurization caused boiling and rapid gold precipitation, mainly in the form of Py3a, Py3b and Py3c, with high gold and arsenic contents. Because of the gradual exhaustion of the ore fluid, the resulting Py3d has low levels of metals (e.g., Au, As, Co, and Ni) relative to Py3a to Py3c (Fig. 10). Finally, due to oxidation of the ore-forming system, previously formed pyrite was partly or completely oxidized to limonite, and only some relicts (Py4) were retained in the late ore stage.

8. Conclusions

Diagenetic pyrite (Py1) and three hydrothermal pyrite (Py2, Py3, and Py4) generations were identified in the Ashawayi gold deposit. The fs–LA–ICP-MS trace element analysis indicates that Py1 was formed by diagenesis in an anoxic to euxinic environment. The early-ore pyrite (Py2) has intermediate geochemical compositions that are between those of typical diagenetic and hydrothermal pyrite and was formed at the incipient introduction of hydrothermal fluid with low As, Au and Cu contents. This hydrothermal fluid may have then reacted with preexisting Py1. The high concentrations of Au and As in Py3 may have come largely from the main ore stage metamorphic fluid, while other trace elements (such as Co and Ni) were released from Py1. Late-ore Py4 occurs as relicts of Py3. The application of a trained artificial neural network classifier to the Ashawayi deposit indicates that the *syn*-ore pyrite has affinities to other orogenic gold deposits in the world. Fluid boiling and fluid-rock/pyrite interactions were the two most important factors for ore metal deposition. This study can serve as a case for exploring the source and precipitation mechanism of ore metals, pyrite classes and their genetic relationships in hydrothermal ore deposits (e.g., epithermal, orogenic and Carlin Au deposits).

Declaration of Competing Interest

The authors declare that they have no known competing financial interests or personal relationships that could have appeared to influence the work reported in this paper.

Data availability

Data will be made available on request.

Acknowledgments

We are grateful to Prof. Chao Zhang and Dr. Wei Xi for helping with the laboratory work, as well as Drs. Xiaohu Wang, Tao Zhang, Ji Ma and Bin Yang for helping with the field investigation. We thank Thomas Ulrich and an anonymous reviewer for their insightful comments and detailed reviews, which improved the quality of this manuscript. We acknowledge Editor Huayong Chen for his very helpful suggestions and efficient handling. This work was jointly supported by the National Natural Science Foundation of China (42172093, 42172258, U1803242 and 41772085), and the National Key Technology Research and Development Program of the Ministry of Science and Technology of China (2021YFC2901904, 2018YFC0604005 and 2015BAB05B04).

Appendix A. Supplementary data

Supplementary data to this article can be found online at https://doi.org/10.1016/j.oregeorev.2023.105452.

References

Abuduxun, N., Xiao, W., Windley, B.F., Chen, Y., Huang, P., Sang, M., Li, L., Liu, X., 2021. Terminal Suturing Between the Tarim Craton and the Yili-Central Tianshan Arc: Insights From Mélange-Ocean Plate Stratigraphy, Detrital Zircon Ages, and Provenance of the South Tianshan Accretionary Complex. Tectonics, 40(7), e2021TC006705.

Abzalov, M., 2007. Zarmitan granitoid-hosted gold deposit, Tianshan belt. Uzbekistan. Econ. Geol. 102 (3), 519–532.

Alexeiev, D.V., Biske, Y.S., Wang, B., Djenchuraeva, A.V., Getman, O.F., Aristov, V.A., Kröner, A., Liu, H.S., Zhong, L.L., 2015. Tectono-Stratigraphic framework and Palaeozoic evolution of the Chinese South Tianshan. Geotectonics 49 (2), 93–122.

Augustin, J., Gaboury, D., 2019. Multi-stage and multi-sourced fluid and gold in the formation of orogenic gold deposits in the world-class Mana district of Burkina Faso-Revealed by LA-ICP-MS analysis of pyrites and arsenopyrites. Ore Geol. Rev. 104, 495–521.

Bajwah, Z.U., Seccombe, P.K., Offler, R., 1987. Trace element distribution Co: Ni ratios and genesis of the big Cadia iron copper deposit, New South Wales. Australia. Mineral. Deposita 22, 292–300.

Bierlein, F.P., Wilde, A.R., 2010. New constraints on the polychromous nature of the giant Muruntau gold deposit from wall-rock alteration and ore paragenetic studies. Aust. J. Earth Sci. 57 (6), 839–854.

Bralia, A., Sabatini, G., Troja, F., 1979. A revaluation of the Co/Ni ration in pyrite as geochemical tool in ore genesis problems. Mineral. Deposita 14, 353–374.

Brown, P.E., 1998. Fluid inclusion modeling for hydrothermal systems. Reviews in Econ. Geol. 10, 151–171.

Charvet, J., Shu, L.S., Laurent-Charvet, S., 2007. Paleozoic structural and geodynamic evolution of eastern Tianshan (NW China): Welding of the Tarim and Junggar plates. Episodes 30 (3), 162–186.

Chen, Y.J., 2006. Orogenic-type deposits and their metallogenic model and exploration potential. Geology in China 33, 1181–1196 in Chinese with English abstract.

Chen, Y.J., 2013. The development of continental collision metallogeny and its application. Acta Petrologica Sinica 29, 1–17 in Chinese with English abstract.

Chen, Y.J., Fu, S.G., 1992. Gold mineralization in West Henan, China. Seismological Press, Beijing 234pp (in Chinese with English abstract).

Chen, H.Y., Chen, Y.J., Baker, M.J., 2012a. Evolution of ore-forming fluids in the Sawayaerdun gold deposit in the Southwestern Chinese Tianshan metallogenic belt. Northwest China. J. Asian Earth Sci. 49, 131–144.

Chen, H.Y., Chen, Y.J., Baker, M.J., 2012b. Isotopic geochemistry of the Sawayaerdun orogenic-type gold deposit, Tianshan, northwest China: Implications for ore genesis and mineral exploration. Chem. Geol. 310–311, 1–11.

Chen, Z.L., Han, F.B., Wang, W., Liu, X.J., Zhang, Q., Zhang, W.G., Zhou, Z.J., Sun, Y., Wang, X.H., Ma, J., Meng, B.D., Liu, Z.R., Ye, L., Huo, H.L., Yang, B., Zhang, T., Wang, C., Du, X.F., Xing, C.H., Zhang, Y.F., 2021. Study on metallogenic regularity and prediction evaluation of superiority mining resource in Southwestern Tianshan Orogen, China, Science Press, Beijing, 383pp (in Chinese).

Chen, B., Hou, Q.L., Feng, H.Y., Guo, H., Xu, Y.X., 2019. Fluid and sulfide component constraints on the genesis and prospecting implications of the Ashawayi gold deposit, South Tianshan, Xinjiang. NW China. Acta Petrologica Sinica 35 (7), 2086–2104 in Chinese with English abstract.

Chen, K., Tian, X.W., Yang, G.R., Zhang, Y.T., 2007. The geological characteristics and exploration guides at the Ashawayi gold deposit. Xinjiang Geology 25 (4), 384–388 in Chinese with English abstract.

Chen, Z.L., Wang, Z.X., Han, F.B., Zhang, W.G., Zhang, Q., Zhou, Z.J., Wang, X.H., Xiao, W.F., Han, S.Q., Yu, X.Q., Sun, Y., Nurgazy, T., Latysheve, N., Zailabidin, H., 2018. Late Cretaceous-Cenozoic uplift, deformation, and erosion of the SW Tianshan Mountains in Kyrgyzstan and Western China. Int. Geol. Rev. 60 (8), 1019–1037.

Chinnasamy, S.S., Hazarika, P., Pal, D., Sen, R., Govindaraj, G., 2021. Pyrite Textures and Trace Element Compositions from the Granodiorite-Hosted Gold Deposit at Jonnagiri, Eastern Dharwar Craton, India: Implications for Gold Mineralization Processes. Econ. Geol. 116 (3), 559–579.

Ciazela, J., Koepke, J., Dick, H.JB.B., R., Muszynski, A., Lazarov, M., Schuth, S., Pieterek, B., Kuhn, Thomas. K.,, 2018. Sulfide enrichment at an oceanic crust-mantle transition zone: Kane Megamullion (23°N, MAR). Geochim. Cosmochim. Acta 230, 155–189.

Cole, A., Wilkinson, J.J., Halls, C., Serenko, T.J., 2000. Geological characteristics, tectonic setting and preliminary interpretations of the Jilau gold-quartz vein deposit. Tajikistan. Mineral. Deposita 35 (7), 600–618.

Cox, S.F., Knackstedt, M.A., Braun, J., 2001. Principles of structural control on permeability and fluid flow in hydrothermal systems. Rev. Econ. Geol. 14, 1–24.

de Boorder, H., 2012. Spatial and temporal distribution of the orogenic gold deposits in the Late Paleozoic Variscides and Southern Tianshan: how orogenic are they? Ore Geol. Rev. 46, 1–31.

Deditius, A.P., Reich, M., Kelser, S.E., Utsunomiya, S., Chryssoulis, S.L., Walshe, J., Ewing, R.C., 2014. The coupled geochemistry of Au and As in pyrite from hydrothermal ore deposits. Geochim. Cosmochim. Acta 140, 644–670.

Deng, X.H., Chen, Y.J., Santosh, M., Wang, J.B., Li, C., Yue, S.W., Zheng, Z., Chen, H.J., Tang, H.S., Dong, L.H., Qu, X., 2017. U-Pb zircon, Re-Os molybdenite geochronology

and Rb-Sr geochemistry from the Xiaobaishitou W (-Mo) deposit: Implications for Triassic tectonic setting in eastern Tianshan. NW China. Ore Geol. Rev. 80, 332–351.
Ding, Q.F., Wu, C.Z., Santosh, M., Fu, Y., Dong, L.H., Qu, X., Gu, L.X., 2014. H-O, S and Pb isotope geochemistry of the Awanda gold deposit in southern Tianshan, Central Asian orogenic belt: Implications for fluid regime and metallogeny. Ore Geol. Rev. 62, 40–52.
Dong, L.H., Feng, J., Qu, X., 2017. Geology of mineral resources in China: the minerogenetic series map of mineral deposits in Xinjiang Uygur Autonomous Region of China (1:, 500000)., 148 pp (in Chinese with English abstract.
Evans, K.A., Phillips, G.N., Powell, R., 2006. Rock-Buffering of Auriferous Fluids in Altered Rocks Associated with the Golden Mile-Style Mineralization, Kalgoorlie Gold Field. Western Australia. Econ. Geol. 101 (4), 805–817.
Fougerouse, D., Micklethwaite, S., Tomkins, A.G., Mei, Y., Kilburn, M., Guagliardo, P., Fisher, L.A., Halfpenny, A., Gee, M., Paterson, D., 2016. Gold remobilization and formation of high grade ore shoots driven by dissolution-reprecipitation replacement and Ni substitution into auriferous arsenopyrite. Geochim. Cosmochim. Acta 178, 143–159.
Frimmel, H.E., 2008. Earth's continental crustal gold endowment. Earth Planet. Sci. Lett. 267 (1–2), 45–55.
Gao, J., He, G.Q., Li, M.S., 1997. Studies on the features of the structural deformations in the western Tianshan orogenic belt. Acta Geoscientia Sinica 18, 1–9 in Chinese with English abstract.
Gao, J., Long, L.L., Klemd, R., Qian, Q., Liu, D.Y., Xiong, X.M., Su, W., Liu, W., Wang, Y. T., Yang, F.Q., 2009. Tectonic evolution of the South Tianshan orogen and adjacent regions, NW China: geochemical and age constraints of granitoid rocks. Int. J. Earth Sci. 98, 1221–1238.
Gao, J., Klemd, R., Qian, Q., Zhang, X., Li, J.L., Jiang, T., Yang, Y.Q., 2011. The collision between the Yili and Tarim blocks of the Southwestern Altaids: geochemical and age constraints of a leucogranite dike crosscutting the HP-LT metamorphic belt in the Chinese Tianshan Orogen. Tectonophysics 499, 118–131.
Garofalo, P.S., Matthäi, S.K., Heinrich, C.A., 2002. Three-dimensional geometry, ore distribution, and time-integrated mass transfer through the quartz-tourmaline-gold vein network of the Sigma deposit (Abitibi belt-Canada). Geofluids 2, 217–232.
Goldfarb, R.J., Groves, D.I., Gardoll, S., 2001. Orogenic gold and geologic time: A global synthesis. Ore Geol. Rev. 18, 1–75.
Goldfarb, R.J., Baker, T., Dube, B., Groves, D.I., Hart, C.J., Gosselin, P., 2005. Distribution, character, and genesis of gold deposits in metamorphic terranes. Economic Geology 100th Anniversary, 407–450.
Goldfarb, R.J., Taylor, R.D., Collins, G.S., Goryachev, N.A., Orlandini, O.F., 2014. Phanerozoic continental growth and gold metallogeny of Asia. Gondwana Res. 25, 48–102.
Graupner, T., Kempe, U., Spooner, E.T.C., Bray, C.J., Kremenetsky, A.A., Irmer, G., 2001. Microthermometric, Laser Raman Spectroscopic, and volatile-ion chromatographic analysis of hydrothermal fluids in the Paleozoic Muruntau Au-bearing quartz vein ore field. Uzbekistan. Econ. Geol. 96, 1–23.
Gregory, D.D., Large, R.R., Halpin, J.A., Baturina, E.L., Lyons, T.W., Wu, S., Danyushevsky, L., Sack, P.J., Chappaz, A., Maslennikov, V.V., Bull, S.W., 2015. Trace element content of sedimentary pyrite in black shales. Econ. Geol. 110, 1389–1410.
Gregory, D.D., Large, R.R., Bath, A.B., Steadman, J.A., Wu, S., Danyushevsky, L., Bull, S. W., Holden, P., Ireland, T.R., 2016. Trace element content of pyrite from the Kapai slate, St. Ives gold district. Western Australia. Econ. Geol. 111, 1297–1320.
Gregory, D.D., Cracknell, M.J., Large, R.R., McGoldrick, P., Kuhn, S., Maslennikov, V.V., Baker, M.J., Fox, N., Belousov, I., Figueroa, M.C., Steadman, J.A., Fabris, A.J., Lyons, T.W., 2019. Distinguishing ore deposit type and barren sedimentary pyrite using laser ablation-inductively coupled plasma-mass spectrometry trace element data and statistical analysis of large data sets. Econ. Geol. 114, 771–786.
Groves, D.I., Goldfarb, R.J., Gebre-Mariam, M., Hagemann, S.G., Robert, F., 1998. Orogenic gold deposits: a proposed classification in the context of their crustal distribution and relationship to other gold deposit types. Ore Geol. Rev. 13 (1–5), 7–27.
Groves, D.I., Goldfarb, R.J., Robert, F., Hart, C.J.R., 2003. Gold deposits in metamorphic belts: Overview of current understanding, outstanding problems, future research, and exploration significance. Econ. Geol. 98, 1–29.
Hagemann, S.G., Luders, V., 2003. P-T-X conditions of hydrothermal fluids and precipitation mechanism of stibnite-gold mineralization at the Wiluna lode-gold deposits, Western Australia: conventional and infrared microthermometric constraints. Mineral. Deposita 38, 936–952.
Han, B.F., He, G.Q., Wang, X.C., Guo, Z.J., 2011. Late Carboniferous collision between the Tarim and Kazakhstan-Yili terranes in the western segment of the South Tian Shan orogen, Central Asia, and implications for the Northern Xinjiang, western China. Earth Sci. Rev. 109 (3–4), 74–93.
Hao, F., Zhou, X.H., Zhu, Y.M., Bao, X.H., Yang, Y.Y., 2009. Charging of the Neogene Penglai 19–3 field, Bohai Bay Basin, China: Oil accumulation in a young trap in an active fault zone. AAPG Bull. 93 (2), 155–179.
Horn, I., von Blanckenburg, F., Schoenberg, R., Steinhoefel, G., Markl, G., 2006. In situ iron isotope ratio determination using UV-femtosecond laser ablation with application to hydrothermal ore formation processes. Geochim. Cosmochim. Acta 70, 3677–3688.
Huang, H., Zhang, Z.C., Kusky, T., Zhang, D.Y., Hou, T., Liu, J.L., Zhao, Z.D., 2012. Geochronology and geochemistry of the Chuanwulu complex in the South Tianshan, western Xinjiang, NW China: Implications for petrogenesis and Phanerozoic continental growth. Lithos 140–141, 66–85.
Huang, H., Wang, T., Qin, Q., Tong, Y., Guo, L., Zhang, L., Hou, J.Y., Song, P., 2015. Geochronology and zircon Hf isotope of Baleigong granitic pluton in the western part of the South Tianshan Mountains: Petrogenesis and implications for tectonic evolution. Acta Petrologica et Mineralogica 34 (6), 971–990 in Chinese with English abstract.
Huo, H.L., 2019. Late Paleozoic tectonic evolution and magmatism of Southwest Tianshan, Northwest China, Unpublished Ph. Chinese Academy of Geological Science, Beijing, China, p. 188 p.. D. thesis,(in Chinese with English abstract.
Huo, H.L., Chen, Z.L., Zhang, Q., Han, F.B., Zhang, W.G., Tang, Y.W., 2019. Chronological constraints on late Paleozoic collision in the southwest Tianshan orogenic belt, China: Evidence from the Baleigong granite. Acta Geol. Sin-Engl. 93 (5), 1188–1204.
Kerr, M.J., Hanley, J.J., Kontak, D.J., Morrison, G.G., Petrus, J., Fayek, M., Zajacz, Z., 2018. Evidence of upgrading of gold tenor in an orogenic quartz-carbonate vein system by late magmatic-hydrothermal fluids at the Madrid Deposit, Hope Bay Greenstone Belt, Nunavut. Canada. Geochim. Cosmochim. Acta 241, 180–218.
Kerrich, R., Goldfarb, R.J., Groves, D.I., Garwin, S., Jia, Y.F., 2000. The characteristics, origins and geodynamic settings of supergiant gold metallogenic provinces. Sci. China Ser. D 43 (Supp.), 1–68.
Konopelko, D., Biske, G., Seltmann, R., Eklun, O., Belyatsky, B., 2007. Hercynian postcollisional A-type granites of the Kokshaal Range, Southern Tien Shan. Lithos 97, 140–160.
Kröner, A., Kovach, V., Belousova, E., Hegner, E., Armstrong, R., Dolgopolova, A., Seltmann, R., Alexeiev, D.V., Hoffmann, J.E., Wong, J., Sun, M., Cai, K., Wang, T., Tong, Y., Wilde, S.A., Degtyarev, K.E., Rytsk, E., 2014. Reassessment of continental growth during the accretionary history of the Central Asian Orogenic Belt. Gondwana Res. 25 (1), 103–125.
Large, R.R., Maslennikov, V.V., Robert, F.O., Danyushevsky, L.V., Chang, Z., 2007. Multistage Sedimentary and Metamorphic Origin of Pyrite and Gold in the Giant Sukhoi Log Deposit, Lena Gold Province. Russia. Econ. Geol. 102 (7), 1233–1267.
Large, R.R., Danyushevsky, L., Hollit, C., Maslennikov, V., Meffre, S., Gilbert, S., Bull, S., Scott, R., Emsbo, P., Thomas, H., Singh, B., Foster, J., 2009. Gold and trace element zonation in pyrite using a laser imaging technique: Implications for the timing of gold in orogenic and Carlin-style sediment hosted deposits. Econ. Geol. 104 (5), 635–668.
Large, R.R., Bull, S.W., Maslennikov, V.V., 2011. A Carbonaceous Sedimentary Source-Rock Model for Carlin-Type and Orogenic Gold Deposits. Econ. Geol. 106 (3), 331–358.
Large, R.R., Halpin, J.A., Danyushevsky, L.V., Maslennikov, V.V., Bull, S.W., Long, J.A., Gregory, D.D., Lounejeva, E., Lyons, T.W., Sack, P.J., McGoldrick, P.J., Calver, C.R., 2014. Trace element content of sedimentary pyrite as a new proxy for deep-time ocean-atmosphere evolution. Earth Planet. Sci. Lett. 389, 209–220.
Li, R.C., Chen, H.Y., Large, R.R., Zhao, L.D., Liu, Y.L., Jiao, J.G., Xia, X.P., Qing, Y., 2020b. Ore-forming fluid source of the orogenic gold deposit: Implications from a combined pyrite texture and geochemistry study. Chem. Geol. 552, 1–17.
Li, X.H., Fan, H.R., Yang, K.F., Hollings, P., Liu, X., Hu, F.F., Cai, Y.C., 2018. Pyrite texture and compositions from the Zhuangzi Au deposit, southeastern North China Craton: Implication for ore-forming processes. Contrib. Mineral. Petrol. 173 (9), 1–20.
Li, P.F., Sun, M., Rosenbaum, G., Cai, K., Yuan, C., Jourdan, F., Xia, X.P., Jiang, Y.D., Zhang, Y.Y., 2020a. Tectonic evolution of the Chinese Tianshan Orogen from subduction to arc-continent collision: Insight from polyphase deformation along the Gangou section, Central Asia. Geol. Soc. Am. Bull. 132, 11–12.
Li, Z.D., Xue, C.J., Xin, J., Wang, S.C., Jia, Z.Y., Shi, G.H., Dong, X.F., Shao, X.L., 2011. Geological Characteristics and S, Pb isotope Geochemistry of Sareke Copper Deposit in Wuqia County. Xinjiang. Geoscience 25 (4), 720–729 in Chinese with English abstract.
Liu, Y., Hu, Z., Gao, S., Günther, D., Xu, J., Gao, C., Chen, H., 2008. In situ analysis of major and trace elements of anhydrous minerals by LA-ICP-MS without applying an internal standard. Chem. Geol. 257, 34–43.
Liu, J.J., Zheng, M.H., Cook, N.J., Long, X.R., Deng, J., Zhai, Y.S., 2007. Geological and geochemical characteristics of the Sawaya'erdun gold deposit, southwestern Chinese Tianshan. Ore Geol. Rev. 32 (1), 125–156.
Mao, J.W., Konopelko, D., Seltmann, R., Lehmann, B., Chen, W., Wang, Y.T., Eklund, O., Usubaliev, T., 2004. Postcollisional age of the Kumtor gold deposit and timing of Hercynian events in the Tien Shan. Kyrgyzstan. Econ. Geol. 99, 1771–1780.
Matthai, S.K., Henley, R.W., Heinrich, C.A., 1995. Gold precipitation by fluid mixing in bedding parallel fractures near carbonaceous slates at the Cosmopolitan Howley gold deposit, Northern Australia. Econ. Geol. 90, 2123–2142.
Mörelli, R., Creaser, R.A., Seltmann, R., Stuart, F.M., Selby, D., Graupner, T., 2007. Age and source constraints for the giant Muruntau gold deposit, Uzbekistan, from coupled Re-Os-He isotopes in arsenopyrite. Geology 35, 795–798.
Peters, K.E., Snedden, J.W., Sulaeman, A., Sarg, J.F., Enrico, R.J., 2000. A new geochemical-sequence stratigraphic model for the Mahakam delta and Makassar slope, Kalimantan. Indonesia. AAPG Bull. 84, 12–44.
Peters, K.E., Ramos, L.S., Zumberge, J.E., Valin, Z.C., Scotese, C.R., Gautier, D.L., 2007. Circum-Arctic petroleum systems identified using decision-tree chemometrics. AAPG Bull. 91, 877–913.
Pitcairn, I.K., Teagle, D.A.H., Craw, D., Olivo, G.R., Kerrich, R., Brewer, T.S., 2006. Sources of metals and fluids in orogenic gold deposits: Insights from the Otago and Alpine Schists, New Zealand. Economic Geology and the Bulletin of the Society of Economic Geologists 101, 1525–1546.
Qiu, Z.J., Fan, H.R., Goldfarb, R., Tomkins, A.G., Yang, K.F., Li, X.C., Xie, L.W., Liu, X., 2021. Cobalt concentration in a sulfidic sea and mobilization during orogenesis: Implications for targeting epigenetic sediment-hosted Cu-Co deposits. Geochim. Cosmochim. Acta 305, 1–18.
Raiswell, R., Berner, R.A., 1985. Pyrite formation in euxinic and semi-euxinic sediments. Am. J. Sci. 285 (8), 710–724.

Reich, M., Kesler, S.E., Utsunomiya, S., Palenik, C.S., Chryssoulis, S.L., Ewing, R.C., 2005. Solubility of Au in arsenian pyrite. Geochim. Cosmochim. Acta 69, 2781–2796.
Rickard, D., 2019. Sedimentary pyrite framboid size-frequency distributions: A meta-analysis. Palaeogeog. Palaeoclimatol. Palaeoecol. 522, 62–75.
Román, N., Reich, M., Leisen, M., Morata, D., Barra, F., Deditius, A.P., 2019. Geochemical and micro-textural fingerprints of boiling in pyrite. Geochim. Cosmochim. Acta 246, 60–85.
Sang, M., Xiao, W.J., Windley, B.F., 2020. Unravelling a Devonian-Triassic seamount chain in the South Tianshan high-pressure/ultrahigh-pressure accretionary complex in the Atbashi area (Kyrgyzstan). Geol. J. 55 (3), 2300–2317.
Seltmann, R., Konopelko, D., Biske, G., Divaev, F., Sergeev, S., 2011. Hercynian post-collisional magmatism in the context of Paleozoic magmatic evolution of the Tien Shan orogenic belt. J. Asian Earth Sci. 42 (5), 821–838.
Sengör, A.M.C., Natalin, B.A., Burtman, V.S., 1993. Evolution of the Altaid tectonic collage and Paleozoic crustal growth in Eurasia. Nature 364, 299–307.
Solomovich, L.I., Trifonov, B.A., 2002. Postcollisional granites in the South Tien Shan Variscan collisional belt. Kyrgyzstan. J. Asian Earth Sci. 21, 7–21.
Tan, Z., Xiao, W., Mao, Q., Wang, H., Sang, M., Li, R., Gao, L.M., Guo, Y.H., Gan, J.M., Liu, Y.H., Wan, B., 2022. Final closure of the Paleo Asian Ocean basin in the early Triassic. Commun. Earth Environ. 3 (1), 1–15.
Taylor, K.G., Macquaker, J.H.S., 2011. Iron minerals in marine sediments record chemical environments. Elements 7 (2), 113–118.
Thomas, H.V., Large, R.E., Bull, S.W., Maslennikov, V., Berry, R.F., Fraser, R., Froud, S., Moye, R., 2011. Pyrite and pyrrhotite textures and composition in sediments, laminated quartz veins, and reefs at Bendigo gold mine, Australia: Insights for ore genesis. Econ. Geol. 106, 1–31.
Ulrich, T., Long, D.G.F., Kamber, B.S., Whitehouse, M.J., 2011. In Situ Trace Element and Sulfur Isotope Analysis of Pyrite in a Paleoproterozoic Gold Placer Deposit, Pardo and Clement Townships, Ontario. Canada. Econ. Geol. 106, 667–686.
Voute, F., Hagemann, S.G., Evans, N.J., Villanes, C., 2019. Sulfur isotopes, trace element, and textural analyses of pyrite, arsenopyrite and base metal sulfides associated with gold mineralization in the Pataz-Parcoy district, Peru: Implication for paragenesis, fluid source, and gold deposition mechanisms. Mineral. Deposita 54, 1077–1100.
Wang, W., Li, W.Y., Tang, X.D., Li, T.H., Xiong, Z.Y., Gao, M.X., Li, T.H., Su, X.H., Guo, Z. P., Meng, Y., Quan, S.C., Chen, C.Q., 2018a. Ore-forming fluid features and mineralization of the Jiashi copper deposit in northwestern Tarim Block. Acta Petrologica et Mineralogica 37 (4), 605–620 in Chinese with English abstract.
Wang, W., Li, W.Y., Tang, X.D., Li, T.H., Xiong, Z.Y., Gao, M.X., Su, X.H., Guo, Z.P., Meng, Y., Quan, S.C., Chen, C.Q., 2018b. Ore-Forming Fluid Features and Mineralization of the Dishui Copper Deposit in the Northwest of Tarim Block. Geology and Exploration 54 (3), 441–455 in Chinese with English abstract.
Wang, C., Liu, L., Luo, J.H., Che, Z.C., Teng, Z.H., Cao, X.D., Zhang, J.Y., 2007. Late Paleozoic post-collisional magmatism in the Southwestern Tianshan orogenic belt, take the Baleigong pluton in the Kokshal region as an example. Acta Petrologica Sinica 23 (8), 1830–1840 in Chinese with English abstract.
Weatherley, D.K., Henley, R.W., 2013. Flash Vapourization during Earthquakes Evidenced by Gold Deposits. Nat. Geosci. 6 (4), 294–298.
Wilson, C.J.L., Schaubs, P., Leader, L.D., 2013. Mineral precipitation in the quartz reefs of the Bendigo gold deposit, Victoria. Australia. Econ. Geol. 108, 259–278.
Winderbaum, L., Ciobanu, C.L., Cook, N.J., Paul, M., Metcalfe, A., d Gilbert, S., 2012. Multivariate analysis of an LA-ICP-MS trace element dataset for pyrite. Math. Geosci. 44 (7), 823–842.
Wu, Y.F., Evans, K., Hu, S.Y., Fougerouse, D., Zhou, M.F., Louise, F.A., Guagliardo, P., Li, J.W., 2021. Decoupling of Au and As during rapid pyrite crystallization. Geology 49 (7), 827–831.
Xiao, W.J., Windley, B.F., Allen, M.B., Han, C.M., 2013. Paleozoic multiple accretionary and collisional tectonics of the Chinese Tianshan orogenic collage. Gondwana Res. 23 (4), 1316–1341.
Xue, C.J., Zhao, X.B., Mo, X.X., Chen, Y.C., Dong, L.H., Gu, X.X., Zhang, Z.C., Nurtaev, B., Pak, N., Li, Z.D., Wang, X.L., Zhang, G.Z., Yaxiaer, Y.L.K., Feng, B., Zu, B., Liu, J.Y., 2014. Tectonic-metallogenic evolution of western Tianshan giant Au-Cu-Zn-Pb metallogenic belt and prospecting orientation. Acta Geologica Sinica 88, 2490–2531 in Chinese with English abstract.
Xue, C.J., Zhao, X.B., Zhao, W.C., Zhao, Y., Zhang, G.Z., Bakhtiar, N., Nikolay, P.A.K., Mo, X.X., 2020. Deformed zone hosted gold deposits in the China-Kazakhstan-Kyrgyzstan-Uzbekistan Tian Shan: metallogenic environment, controlling parameters, and prospecting criteria. Earth Science Frontiers 27 (2), 294–319 in Chinese with English abstract.
Yang, F.Q., Mao, J.W., Wang, Y.T., Zhao, C.S., Zhang, Y., Liu, Y.L., 2007. Major types, characteristics and metallogenesis of gold deposits in southwest Tianshan Mountains. Xinjiang. Mineral Deposits 26 (4), 361–379 in Chinese with English abstract.
Yang, L., Wang, Q.F., Large, R.R., Mukherjee, I., Deng, J., Li, H.J., Yu, H.Z., Wang, X., 2021. Fluid source and metal precipitation mechanism of sediment-hosted Chang'an orogenic gold deposit, SW China: Constraints from sulfide texture, trace element, S, Pb, and He-Ar isotopes and calcite C-O isotopes. Am. Mineral. 106 (3), 410–429.
Zhang, T., Chen, Z.L., Huang, H.Y., Zhang, W.G., Zhang, Q., Pan, J.Y., Zhou, Z.J., Zou, M. L., Feng, H.Y., Wang, X., H., Han, F.B., Sun, Y., Huo, H.L., Ma, J., Yang, B., 2020. Geochemical characteristics of gold-bearing minerals and its geological significance in the Ashawayi gold deposit in the southwestern Tianshan Orogen. Journal of Geomechanics 26 (3), 443–458 in Chinese with English abstract.
Zhang, T., Chen, Z.L., Zhou, Z.J., Zhang, W.G., Zhang, Q., Pan, J.Y., Han, F.B., Sun, Y., Feng, H.Y., Ma, J., Yang, B., 2021. Geochemical characteristics of fluid inclusions and H-O isotopes of the Ashawayi gold deposit in Southwest Tianshan Orogen and its orogenic-type gold deposit, 002.html (in Chinese with English abstract Geology in China. https://kns.cnki.net/kcms/detail/11.1167.P.20210226.1949.
Zhang, C.L., Xu, Y.G., Li, Z.X., Wang, H.Y., Ye, H.M., 2010. Diverse Permian magmatism in the Tarim block, NW China: Genetically linked to the Permian Tarim mantle plume? Lithos 119, 537–552.
Zhang, G.Z., Xue, C.J., Chi, G.X., Liu, J.Y., Zhao, X.B., Zu, B., Zhao, Y., 2017. Multiple-stage mineralization in the Sawayaerdun orogenic gold deposit, western Tianshan, Xinjiang: Constraints from paragenesis, EMPA analyses, Re-Os dating of pyrite (arsenopyrite) and U-Pb dating of zircon from the host rocks. Ore Geol. Rev. 81, 326–341.
Zhao, R.F., Yang, J.G., Wang, M.C., Yao, W.G., 2002. The study of metallogenic geologic setting and prospecting potential evaluation in South-western Tianshan Mountains. North-western Geology 35, 101–121 in Chinese with English abstract.
Zhao, L.T., Zhu, X.Y., Li, S.H., Huang, X.K., 2018. Geological and C-H-O-S isotope geochemical characteristics of Sareke copper deposit in Xinjiang. Mineral Resources and Geology 32 (1), 18–26 in Chinese with English abstract.
Zhong, R.C., Deng, Y., Li, W.B., Danyushevsky, L.V., Cracknell, M.J., Belousov, I., Chen, Y.J., Li, L.M., 2021. Revealing the multi-stage ore-forming history of a mineral deposit using pyrite geochemistry and machine learning-based data interpretation. Ore Geol. Rev. 133, 104079.
Zhou, Z.J., Chen, Y.J., Jiang, S.Y., Zhao, H.X., Qin, Y., Hu, C.J., 2014a. Geology, geochemistry and ore genesis of the Wenyu gold deposit, Xiaoqinling gold field, southern margin of North China Craton. Ore Geol. Rev. 59, 1–20.
Zhou, Z.J., Liu, Z.W., Qin, Y., 2014b. Geology, geochemistry and genesis of the Huachanggou gold deposit, western Qinling Orogen, central China. Geol. J. 49, 424–441.
Zhou, Z.J., Chen, Y.J., Jiang, S.Y., Hu, C.J., Qin, Y., Zhao, H.X., 2015. Isotope and fluid inclusion geochemistry and ore genesis of the Qiangma gold deposit, Xiaoqinling gold field, Qinling Orogen, southern margin of North China Craton. Ore Geol. Rev. 66, 47–64.
Zhou, Z.J., Chen, Z.L., Han, F.B., Han, S.Q., Wang, Z.X., Xiao, W.F., Shen, T., Wu, J.F., 2018. Fluid inclusion and isotope geochemistry of the Atebayue Sb deposit, South Tianshan Orogen. Kyrgyzstan. Geol. J. 53, 1050–1060.
Zhou, Z.J., Chen, Z.L., Nurtaev, B., Shukurov, S., Han, F.B., Wang, Z.X., Xiao, W.F., Yu, X. Q., 2019. Re-Os Geochronology and Sulfur Isotopes of the Lyangar W-Mo Deposit: Implications for Permian Tectonic Setting in South Tianshan Orogen. Uzbekistan. Minerals 9 (9), 534.
Zhou, Z.J., Chen, Z.L., Zhang, W.G., Huo, H.L., Liu, B., Yan, Q.J., Li, J.L., 2022. Geology, C-H-O isotopes, and muscovite ^{40}Ar-^{39}Ar dating of the Qingbaishan gold deposit: Implications for tectonism and metallogenesis of early Devonian gold deposits in the Beishan orogen. NW China. Ore Geol. Rev. 145, 104895.